

1 This is a post-peer-review, pre-copyedit version of an article published in Ore Geology Reviews.

2 The final authenticated version is available online at:

3 <http://dx.doi.org/10.1016/j.oregeorev.2016.11.030>

4

5 **The Cogne magnetite deposit (Western Alps, Italy): a Late Jurassic seafloor ultramafic-**  
6 **hosted hydrothermal system?**

7

8 Luca Toffolo<sup>1,\*</sup>, Paolo Nimis<sup>1</sup>, Silvana Martin<sup>1</sup>, Simone Tumiati<sup>2</sup>, Wolfgang Bach<sup>3</sup>

9

10 <sup>1</sup> Geosciences Department, University of Padua, via Gradenigo 6, 35100 Padua, Italy,

11 [luca.toffolo@phd.unipd.it](mailto:luca.toffolo@phd.unipd.it), [paolo.nimis@unipd.it](mailto:paolo.nimis@unipd.it), [silvana.martin@unipd.it](mailto:silvana.martin@unipd.it)

12 <sup>2</sup> Earth Sciences Department, University of Milan, via Mangiagalli 34, 20133 Milan, Italy,

13 [simone.tumiati@unimi.it](mailto:simone.tumiati@unimi.it)

14 <sup>3</sup> Department of Geosciences and MARUM Center for Marine Environmental Sciences, P.O. Box

15 330440, 28334 Bremen, Germany, [wbach@uni-bremen.de](mailto:wbach@uni-bremen.de)

16

17 \* Corresponding author.

18

19 **ABSTRACT**

20

21 The Cogne magnetite deposit (Western Alps, Italy) is the largest in a series of apatite and sulphide-  
22 free magnetite orebodies that are hosted in serpentinites belonging to western Alpine ophiolitic units.

23 The nearly endmember composition of magnetite, which is unusual for an ultramafic setting, and the  
24 relatively high tonnage of the deposit ( $18 \cdot 10^6$  tonnes at 45-50 wt% Fe) make Cogne an intriguing  
25 case study to explore magnetite-forming processes in ophiolites. The Cogne magnetite shows variable  
26 textures, including nodular ores, veins and fine-grained disseminations in serpentinites after tectonic

27 peridotites and totally serpentinized melt-impregnated peridotites (troctolites). An increase in Co/Ni  
28 ratio from magnetite-poor serpentinized peridotites (0.05) to nodular magnetite ores (>1) is observed.  
29 Trace element analyses of magnetite from different sites and lithologies by laser-ablation inductively-  
30 coupled mass spectrometry indicate that magnetites have typical hydrothermal compositions,  
31 characterized by high Mg and Mn (median values up to ~24100 and ~5000 ppm, respectively), and  
32 low Cr, Ti and V (median values up to ~30, ~570 and ~60 ppm, respectively). Moreover, the  
33 variations in trace element compositions distinguish magnetite that is hydrothermal fluid-controlled  
34 [highest (Mg, Mn, Co, Zn)/Ni ratios] from magnetite whose composition is affected by host-rock  
35 chemistry (highest Ni  $\pm$  Ti  $\pm$  V). U-Th-Pb dating of magnetite-associated uraninite constrains the  
36 formation of the deposit to the Late Jurassic (ca. 150 Ma), during an advanced stage of the opening  
37 of the Alpine Tethys. Thermodynamic modelling of fluid-rock interactions indicates that fluids  
38 produced by seawater-peridotite or seawater-Fe-gabbro are not sufficiently Fe-rich to account for  
39 the formation of the Cogne deposit. This suggests that fractionation processes such as phase  
40 separation were critical to generate hydrothermal fluids capable to precipitate large amounts of  
41 magnetite in various types of ultramafic host-rocks. The oceanic setting and geochemical and  
42 mineralogical similarities with some modern ultramafic-hosted volcanogenic massive sulphide  
43 deposits on mid-ocean ridges suggest that the exposed mineralized section at Cogne may represent  
44 the deep segment of a seafloor, high-temperature (~300–400°C) hydrothermal system. The  
45 occurrence of similar magnetite enrichments in present-day oceanic settings could contribute to  
46 explain the presence of significant magnetic anomalies centred on active and inactive ultramafic-  
47 hosted hydrothermal fields.

48

## 49 **1. Introduction**

50

51 The Cogne mining district (southern Valle d'Aosta region, Western Alps, Italy; Fig. 1) consists of a  
52 set of mines, which exploited a magnetite-rich serpentinite unit from the Middle Ages to 1979. The  
53 tonnage of the ore deposit was estimated at 18 Mt (Nazionale "Cogne" S.p.a., 1954), and the run-of-  
54 mine ore produced in the 1960s had an iron grade of 45-50% (Di Colbertaldo et al., 1967). The Cogne  
55 deposit is the largest in a series of apatite and sulphide-free serpentinite-hosted magnetite orebodies  
56 that crop out in ophiolitic units along the western Alpine collisional suture in Valle d'Aosta (Castello,  
57 1981; Diella et al., 1994; Rossetti et al., 2009; Stella, 1921) and in its southern extension in Corsica  
58 (Farinole mine; Routhier, 1963). In southern Valle d'Aosta, most of these magnetite orebodies occur  
59 in the Mt. Avic serpentinite massif (located ca. 15 km ENE of the Cogne serpentinite; Fig. 1) and  
60 have been interpreted as former metasomatized podiform chromitites, based on their high Cr  
61 concentration and the presence of chromite relicts (Diella et al., 1994; Della Giusta et al., 2011;  
62 Rossetti et al., 2009). A similar origin has been proposed for analogous Mesozoic (probably Jurassic),  
63 ophiolite-hosted magnetite deposits in Greece (Vermion, Olympus and Edessa regions and Skyros  
64 island; Paraskevopoulos and Economou, 1980). The Cogne deposit differs from the above  
65 occurrences because its magnetite has a nearly pure endmember composition and contains only trace  
66 amounts of compatible elements such as Cr, Ti and V (Carbonin et al., 2014; Compagnoni et al.,  
67 1981). This geochemical fingerprint, which is unusual for an ultramafic setting, as well as the  
68 relatively high tonnage of the deposit, make Cogne an interesting and still poorly studied example of  
69 ophiolite-hosted magnetite deposit. Understanding its genesis may have implications for our  
70 interpretation of magnetic anomalies reported from modern ultramafic-hosted hydrothermal sites on  
71 slow-spreading mid-ocean ridges (Fujii et al., 2016; Szitkar et al., 2014; Tivey and Dymant, 2010).

72 Several hypotheses have been put forward to explain the genesis of the Cogne deposit. Di  
73 Colbertaldo et al. (1967) proposed a genesis by magmatic segregation from an ultramafic melt. Based  
74 on the Cr and Ti-poor composition of the magnetite, Compagnoni et al. (1979, 1981) ascribed the

75 formation of the Cogne magnetite to high-temperature serpentinization of oceanic peridotites and  
76 consequent Fe mobilization, but they did not discuss this hypothesis in detail. Recently, Carbonin et  
77 al. (2014) investigated some of the magnetite-associated lithologies and suggested their possible  
78 hydrothermal origin; however, the ore-forming processes were not explored.

79 In this paper, we present new petrographic and geochemical data on the Cogne deposit, focusing  
80 on the textural relationships and the trace element composition of magnetite. The latter has been a  
81 valuable tool in the identification of the petrogenetic environment (e.g., Boutroy et al., 2014; Dare et  
82 al., 2014; Dupuis and Beaudoin, 2011; Nadoll et al., 2014; Nadoll et al., 2015). In addition, we  
83 determine for the first time the radiometric age of the magnetite orebody by U–Th–Pb dating of  
84 uraninite. We will show that the magnetite geochemistry and age support a seafloor oceanic  
85 hydrothermal setting for the Cogne deposit, and we will explore the possible formation mechanisms,  
86 using constraints from geochemical modelling of seawater-rock reactions.

87

## 88 **2. Geology of the Cogne mining area**

89

90 The Cogne serpentinite is a 2.5 km long sliver, with an average thickness of 100 m (Di Colbertaldo  
91 et al. 1967), which is exposed on the S and W slopes of Montzalet (Fig. 1 and 2). The serpentinite is  
92 tectonically sandwiched between two different metasedimentary sequences. The foot wall sequence  
93 consists of tectonically juxtaposed slivers of calcschists, marbles, dolomitic marbles and quartzites  
94 formed in a continental margin and in other paleogeographic domains (Cogne Unit; Polino et al.,  
95 2014). The hanging wall sequence is represented by calcschists, marbles and minor, Fe- and Mn-  
96 bearing metacherts. The basal contact of the serpentinite is a thrust fault (Elter, 1971), while the upper  
97 limit is marked by a few cm- to 3 m-thick boudinaged rodingite, which we tentatively interpret as a  
98 tectonically activated, primary serpentinite-sediment interface. According to Elter (1971), the Cogne  
99 serpentinite and the hanging wall metasediments form the core of a km-scale isoclinal fold that repeats  
100 the Cogne unit in its upper limb (Fig. 2b). The Cogne serpentinite and the hanging wall metasediments

101 are considered to be part of the same greenschist- to blueschist-facies ophiolite-bearing unit  
102 (Aouilletta Unit; Polino et al., 2014), which is sandwiched together with the foot wall marbles and  
103 quartzites between two eclogite-facies ophiolitic units (Grivola-Urtier Unit and Zermatt-Saas Unit;  
104 Dal Piaz et al., 2010). These ophiolitic units are remnants of the Jurassic Piedmont-Liguria ocean  
105 (Alpine Tethys; Schmid et al., 2004; Stampfli, 2000). From Late Cretaceous to Eocene, these  
106 ophiolitic units followed different P-T paths related to their subduction beneath the Adriatic micro-  
107 plate, as a result of Africa-Europe convergence (Schmid et al., 2004). In the Zermatt-Saas Unit (in  
108 southern Valle d'Aosta), the high-pressure (eclogitic) metamorphic peak was reached in the Eocene  
109 (45-42 Ma; Dal Piaz et al., 2001), contemporaneously with the closure of the ocean (Dal Piaz et al.,  
110 2003), and was followed by a greenschist-facies overprint during Late Eocene-Early Oligocene (Dal  
111 Piaz et al., 2001, 2003). No P-T-time estimate is available for the Cogne serpentinite and its host  
112 Aouilletta Unit.

113 The Cogne magnetite mineralization is confined to the serpentinite body (Compagnoni et al.,  
114 1979; Di Cobertaldo et al., 1967) and it is exposed in three zones, henceforward referred to as Site 1,  
115 Site 2 and Site 3 (Fig. 2). At Site 1 (which includes the mines of Liconi, 45.612509 N 7.395377 E,  
116 Colonna, 45.609716 N 7.391322 E, and Costa del Pino, 45.610466 N 7.378247 E), the orebody is a  
117 50-70 m-thick, 600 m-long continuous lens that dips and wedges out northward (Di Colbertaldo et  
118 al., 1967). This orebody was extensively exploited in the second half of the twentieth century by  
119 sublevel caving. At Site 2 (western slope of Montzalet, 45.618124 N 7.386316 E) and Site 3 (Larsinaz  
120 mine, 45.619119 N 7.377135 E), the intensely mineralized rock volumes are much smaller, and  
121 consist of disseminations and veins at Site 2 and of a less than 10 m-thick lens at Site 3 (Stella, 1916).  
122 The mineralized serpentinite was subjected to only low degrees of Alpine deformation and  
123 metamorphism (Carbonin et al., 2014), which allowed extensive preservation of the original  
124 structures (see below).

125

126

## 127 **3. Materials and methods**

128

### 129 *3.1. Petrographic and mineralogical analysis*

130

131 Sixty-eight rock samples from the Cogne mining area were collected from mine dumps and outcrops  
132 and studied by means of optical microscopy in thin polished sections. No potential source of lead was  
133 present during any stage of the sample preparation, to avoid contamination that could invalidate the  
134 subsequent geochronological analyses. Mineral identification was aided by micro-Raman  
135 spectroscopy, using a Thermo Scientific™ DXR™ confocal Raman system at the Chemistry  
136 Department of the University of Padua (Italy). We chose a 532 nm laser working at a power of 5-10  
137 mW. All of the Raman spectra were collected with a 50x LWD objective lens, reaching a spatial  
138 resolution of ~1 µm. Raman spectroscopy was crucial for the identification of serpentine minerals,  
139 for which we followed the guidelines by Groppo et al. (2006) and Carbonin et al. (2014). Selected  
140 samples were further investigated using a scanning electron microscope (SEM). Back-scattered  
141 electron images were obtained using a CamScan MX 2500 SEM at the Department of Geosciences  
142 of the University of Padua (Italy) equipped with a LaB<sub>6</sub> crystal, working at 20 kV accelerating voltage  
143 and 140 nA current.

144 Mineral compositions of major minerals were determined by electron microprobe analysis  
145 (EPMA) using a CAMECA SX-50 electron microprobe, equipped with four WDS spectrometers and  
146 one EDS spectrometer, at IGG-CNR, Padua (Italy). The K $\alpha$  emission lines of ten elements (Na, Mg,  
147 Al, Si, K, Ca, Ti, Cr, Mn, Fe) were measured using the following natural and synthetic minerals and  
148 oxides as standards: albite (Na), diopside (Si, Ca), orthoclase (K), MgO, Al<sub>2</sub>O<sub>3</sub>, MnTiO<sub>3</sub>, Cr<sub>2</sub>O<sub>3</sub> and  
149 Fe<sub>2</sub>O<sub>3</sub>. Working conditions were 20 kV, 20 nA, 10 s for peak and 5 s for the background on each side  
150 of the peak.

151

### 152 *3.2. Bulk rock compositions*

153

154 Fourteen rock samples, representative of the main lithologies encountered in and around the deposit,  
155 were analysed for major, minor and selected trace elements by X-ray fluorescence (XRF). The  
156 samples were prepared as fine powder by means of a Retsch M0 agate mortar grinder and a Retsch  
157 RS100 vibratory disk mill, equipped with agate disks. The powder samples, fused into beads, were  
158 then analysed using a Philips PW2400 XRF wavelength-dispersive sequential spectrometer equipped  
159 with a Rh tube at the Department of Geosciences of the University of Padua (Italy). Reference  
160 standards were natural geological samples (Govindaraju, 1994). The relative analytical precision is  
161 estimated to within  $\pm 0.6\%$  for major and minor elements and within  $\pm 3\%$  for trace elements. The  
162 relative accuracy is within  $\pm 0.5\%$  for Si,  $\pm 3\%$  for the other major and minor elements, and  $\pm 5\%$  for  
163 trace elements. Detection limits are better than 0.01 wt% for Al, Mg and Na, 0.2 wt% for Si and 0.005  
164 wt% for Ti, Fe, Mn, Ca, K and P. For trace elements, the detection limits are 3 ppm for Co, Ni, Cu,  
165 Zn, Rb, Sr, Y, Zr, Nb, Th, and U, 5 ppm for Sc, V, Ga, and Pb, 6 ppm for Cr, and 10 ppm for Ba, La,  
166 Ce, and Nd.

167 The geochemistry of seven whole-rock samples was further investigated by inductively coupled  
168 plasma mass spectrometry and emission spectroscopy (ICP-MS/ES) analyses, which were performed  
169 by Bureau Veritas Mineral Laboratories (Canada). The pulverised rock samples were mixed with  
170  $\text{LiBO}_2/\text{Li}_2\text{B}_4\text{O}_7$  flux and fused. The cooled beads were then digested with ACS grade nitric acid. The  
171 detection limits for trace elements are: 1 ppm for Be, Sc, Sn, and Ba; 8 ppm for V; 14 ppm for Cr;  
172 0.2 ppm for Co and Th; 20 ppm for Ni; 0.5 ppm for Ga, Sr and W; 0.1 ppm for Y, Zr, Nb, Cs, Hf, Ta,  
173 U, La, Ce; 0.3 ppm for Nd.

174

### 175 *3.3. U-Th-Pb dating*

176

177 Thirteen thin sections of magnetite ore were scanned for uraninite crystals by back-scattered electron  
178 imaging with a Scanning Electron Microscope (SEM). Four of these samples showed uraninite grains

179 of sufficient size to allow their chemical analysis by EPMA and successive dating by the U-Th-Pb  
180 method. Uraninite compositions were measured at the Department of Earth Sciences of the University  
181 of Milan (Italy), using a JEOL JXA-8200 electron microprobe equipped with five WDS and one EDS  
182 spectrometers. An accelerating voltage of 15 kV and a beam current intensity of 20 nA were used.  
183 Nine elements were measured by WDS spectrometry using the following X-ray lines:  $MgK\alpha$ ,  $SiK\alpha$ ,  
184  $TiK\alpha$ ,  $CaK\alpha$ ,  $CrK\alpha$ ,  $FeK\alpha$ ,  $UM\beta$ ,  $ThM\alpha$  and  $PbM\alpha$ . The counting time was 60 s for the peak and 30 s  
185 for the background for all analysed elements. The standards were olivine (Mg), grossular (Si and Ca),  
186 ilmenite (Ti), fayalite (Fe), pure Cr and synthetic  $UO_2$ ,  $ThO_2$  and  $PbO$ . Detection limits for elements  
187 relevant to geochronology are 290 ppm for U, and 170 ppm for Th and Pb. Relative errors (relative  
188 standard errors) of 0.1%, 0.5% and 0.7% for U, Th and Pb concentrations, respectively, were  
189 calculated on the basis of 5 repetitions of the same measurement. However, a more realistic minimum  
190 relative error for U, Th and Pb concentrations >7500 ppm is 2% (Cocherie and Albarede, 2001).

191 Chemical maps were preliminarily acquired on the uraninite grains to assess the presence of  
192 chemical zoning. In order to collect a significant amount of data, we performed both single spot  
193 analyses and automated traverses. The latter method allowed us to obtain a large number of data  
194 points, although the proportion of mixed or poor-quality analyses increased. Thus, prior to calculating  
195 ages, we excluded the analyses which showed obvious contaminations, low totals or anomalously  
196 low Pb contents, if compared to adjacent points in the same traverse.

197 The possibility of dating uraninite with EPMA was discussed by Bowles (1990) and calculated  
198 ages were demonstrated to be accurate and consistent with independent isotopic measurements  
199 (Bowles, 2015; Cross et al., 2011). According to Bowles (2015), the best accuracy is obtained for  
200 ages from ~2 Ma to 700-1000 Ma: the lower limit is imposed by the EPMA detection limit of Pb and  
201 the upper limit is linked to metamictization of the uraninite crystal lattice, which may lead to Pb loss.  
202 Meaningful ages are obtained if the initial concentration of non-radiogenic Pb is negligible and the  
203 U-Th-Pb system remained closed after uraninite crystallization. The former assumption is considered



204 to hold true because  $\text{Pb}^{2+}$  is incompatible in the uraninite crystal structure (Alexandre and Kyser,  
205 2005), whereas the latter assumption needs to be assessed by careful sample examination.

206 The formula used to calculate the age  $t$  (in years) is (Montel et al., 1996):

$$\begin{aligned} 207 \quad \text{Pb} = & 208(\text{Th}/232) \cdot [\exp(\lambda^{232} \cdot t) - 1] + 206(\text{U}/238.04) \cdot [1 - ({}^{235}\text{U}/{}^{238}\text{U})] \cdot [\exp(\lambda^{238} \cdot t)] + \\ 208 \quad & + 207(\text{U}/238.04) \cdot ({}^{235}\text{U}/{}^{238}\text{U}) \cdot [\exp(\lambda^{235} \cdot t)], \end{aligned}$$

209 where Th and U are the measured concentrations in ppm,  $\lambda^{232}$ ,  $\lambda^{238}$ ,  $\lambda^{235}$  are the decay constants of  
210  ${}^{232}\text{Th}$ ,  ${}^{238}\text{U}$  and  ${}^{235}\text{U}$ , respectively, and  ${}^{235}\text{U}/{}^{238}\text{U}$  is the bulk Earth's uranium isotopic ratio. The values  
211 used in the calculations are:  $\lambda^{232} = 4.9475 \cdot 10^{-11} \text{ a}^{-1}$  (LeRoux and Glendenin, 1963);  $\lambda^{238} = 1.55125 \cdot 10^{-10}$   
212  $\text{a}^{-1}$  and  $\lambda^{235} = 9.8485 \cdot 10^{-10} \text{ a}^{-1}$  (Jaffey et al., 1971);  ${}^{235}\text{U}/{}^{238}\text{U} = 0.0072559$  (Hiess et al., 2012). To  
213 obtain an initial guess of  $t$  we used the formula (modified from Bowles, 2015):

$$214 \quad t = (1/\lambda^{238}) \cdot \ln (1 + \text{Pb}/\{[1 - ({}^{235}\text{U}/{}^{238}\text{U})] \cdot 206(\text{U}/238.04)\}).$$

215 Then the difference between the calculated and the measured values of Pb is minimized by least-  
216 squares method, varying  $t$ . Whenever possible, ages were obtained as weighted averages of several  
217 analyses, after outlier rejection based on a modified  $2\sigma$  set of criteria (Ludwig, 2012).

218

### 219 *3.4. Trace elements in magnetite*

220

221 Trace elements in magnetite were measured by laser-ablation inductively-coupled plasma mass  
222 spectrometry (LA-ICP-MS) at the Petrology of the Ocean Crust Laboratory, University of Bremen  
223 (Germany), using a high-resolution double-focussing ThermoFinnigan Element2, equipped with a  
224 solid-state laser with a wavelength of 193 nm (New Wave UP193). Magnetite grains were analysed  
225 on standard thin polished sections using a 35  $\mu\text{m}$  laser spot size, a pulse frequency of 5 Hz, an  
226 irradiance at the sample of  $\sim 1.3 \text{ GW}/\text{cm}^2$  and an acquisition time of 60 s, comprehensive of 25 s for  
227 background measurement. To avoid any risk of contamination on the surface of the rock section, the  
228 zone to be investigated was pre-ablated using two laser pulses with 50  $\mu\text{m}$  spot size. The analysed

229 elements ( $^{25}\text{Mg}$ ,  $^{29}\text{Si}$ ,  $^{43}\text{Ca}$ ,  $^{47}\text{Ti}$ ,  $^{51}\text{V}$ ,  $^{53}\text{Cr}$ ,  $^{55}\text{Mn}$ ,  $^{57}\text{Fe}$ ,  $^{59}\text{Co}$ ,  $^{60}\text{Ni}$ ,  $^{66}\text{Zn}$ ,  $^{90}\text{Zr}$ ,  $^{98}\text{Mo}$ ) were measured in  
230 low-resolution mode in order to shorten the acquisition time, although preserving high counts per  
231 second (cps). We opted for this configuration to avoid deep ablation pits, thus reducing the probability  
232 of hitting inclusions or adjacent minerals. The Fe concentration of magnetite as determined by EPMA  
233 was used as an internal standard. External standards (reference materials NIST61, BCR-2G and  
234 BHVO) were analysed under the same conditions as the samples every 5 to 9 analyses during the  
235 same session, in order to check for possible drift. Signal files, reporting intensities (cps) vs. time,  
236 were inspected for possible heterogeneities related to the presence of inclusions and chemical zoning.  
237 Integration of the signal and calculation of concentrations were performed with the GeoPro<sup>TM</sup>  
238 software (CETAC Technologies). Detection limits (DL) were calculated on reference materials using  
239 the formula:

$$240 \quad DL_i = [3\sqrt{2}S_{bkgd}/(\bar{X}_{sgl} - \bar{X}_{bkgd})] \cdot C_i,$$

241 where  $i$  is the  $i^{\text{th}}$  element,  $S_{bkgd}$  is the sample standard deviation of the background (in cps),  $\bar{X}_{sgl}$  and  
242  $\bar{X}_{bkgd}$  are the average signal and the background (in cps) respectively, and  $C_i$  is the concentration (in  
243 ppm) of the  $i^{\text{th}}$  element in the reference materials.

244 The statistical relationships between chemical elements in magnetite were explored by robust  
245 principal component analysis (PCA), using the function “pcaCoDa” in the “robCompositions” library  
246 for R software (Templ et al., 2011). Robust PCA was preferred to “classical” PCA because it is less  
247 sensible to outliers (Filzmoser et al., 2009; Filzmoser and Hron, 2011). Four analyses (out of ninety-  
248 four) with V contents below the detection limit were excluded from calculations.

249

### 250 *3.5. Geochemical modelling*

251

252 In an attempt to simulate the genesis of the Cogne deposit in a seafloor hydrothermal model system,  
253 fluid-rock interactions were modelled with the EQ3/6 (Version 8.0a) software package (Wolery,  
254 2013), using the database compiled by Klein et al. (2009), which contains thermodynamic properties

255 of minerals and solutes in the 0-400°C range at the fixed pressure of 500 bar. The database was  
256 modified to include revised data for  $\text{HCl}_{(\text{aq})}$  (Ho et al., 2001),  $\text{NaCl}_{(\text{aq})}$  (Ho et al., 1994),  $\text{KCl}_{(\text{aq})}$  (Ho  
257 et al., 2000),  $\text{FeCl}_{2(\text{aq})}$  and  $\text{FeCl}^+_{(\text{aq})}$  (Ding and Seyfried, 1992). The modelling procedure, which in  
258 the first steps follows that of Klein et al. (2009), is described below.

259 First, 1 kg of modern seawater (Table 1; composition from Klein et al., 2009) is speciated at  
260 25°C and 1 bar. Then, seawater is heated and reacted with 1 g of fresh harzburgite (Table 2) in a  
261 closed system to the desired temperature (at  $P = 500$  bar), to simulate a downward fluid path towards  
262 the reaction zone (Klein et al., 2009). The chosen pressure of 500 bar simulates conditions at ~2000  
263 m below seafloor, which do not exceed the reported depth of magma chambers fuelling hydrothermal  
264 fields on slow-spreading ridges (~3 km; Singh et al., 2006), assuming a 3000-m water column, which  
265 is a typical value for modern slow-spreading ridge hydrothermal systems (Edmonds, 2010). All the  
266 produced minerals are removed at the end of the run, because in a real fluid pathway they would be  
267 left behind by downwelling seawater. A positive effect of this step is to narrow down the  $f_{\text{O}_2}$  range in  
268 following calculations, thus improving the code stability (Wolery and Jarek, 2003). In the successive  
269 step, which simulates a reaction zone, 1 kg of the resulting hydrothermal fluid is reacted at 400°C  
270 with an increasing amount of either fresh harzburgite or Fe-gabbro (Table 2) in a closed system  
271 (Wolery and Jarek, 2003). We chose the temperature of 400°C because it maximizes Fe solubility,  
272 which is strongly temperature-dependent (Seyfried et al., 2004), and is also compatible with estimates  
273 of fluid temperatures in modern subseafloor reaction zones ( $T > 375^\circ\text{C}$ , Berndt et al., 1989;  $T \sim 400^\circ\text{C}$   
274 based on the maximum amount of heat that water can carry by buoyancy-driven advection, Jupp and  
275 Schultz, 2004 and references therein) and with measured temperatures of modern seafloor vent fluids  
276 (e.g., Edmonds, 2010). The reaction path is terminated after the maximum value of dissolved Fe is  
277 reached. Finally, the Fe-rich hydrothermal fluid is titrated in a closed system with selected lithologies  
278 (Table 2) at 300°C or 400°C, in accordance with the temperature range estimated for hydrothermal  
279 mineral assemblages by Carbonin et al. (2014). The equilibrium mineral assemblages and the relative  
280 abundances of the phases obtained for different water/rock (W/R) ratios are then compared to those

281 observed in the natural rocks. The model does not account for solid solutions, hence, by suppressing  
282 Fe-Mg exchange in secondary phases, it maximises the extent of magnetite production.

283

284

## 285 **4. Results**

286

### 287 *4.1. Petrographic features of the magnetite ores and mineral compositions*

288

289 The Cogne magnetite ore is heterogeneous in terms of texture and gangue mineral assemblage. Three  
290 main textural types of magnetite ore are distinguished, which are termed here *nodular*, *fine-grained*  
291 *disseminated* and *vein*.

292 The nodular ores (Fig. 3a, b) are characterized by mm to cm-sized magnetite crystals in a silicate  
293 matrix, giving the rock a macroscopic appearance similar to that of nodular chromitites. The nodular  
294 textures show a continuum between three major subtypes, which are termed here *leopard*, *harrisitic*  
295 and *massive* subtype, respectively. In the leopard subtype, the magnetite crystals, which mostly  
296 consist of aggregates of subgrains, are subrounded and constitute up to 50 vol% of the rock. In the  
297 harrisitic subtype, the magnetite crystals form up to 10 cm-long rods, mimicking the texture shown  
298 by dendritic olivine in harrisite. In the massive subtype, the magnetite content is as high as 80-90  
299 vol%, but subrounded crystals similar to those of the nodular ores are still recognizable.

300 The fine-grained disseminated ores consist of bands in the host-rock, which contain variable  
301 proportions of sub-millimetric magnetite grains (up to ~70 vol). The vein ores (Fig. 3c) are cm-thick,  
302 dismembered veins composed of magnetite, chalcopyrite and antigorite; the proportion of opaque  
303 minerals over the associated silicates is ~50 vol%.

304 Since the distribution of the different ore types is not uniform across the deposit, we will treat  
305 each sampling site separately.

306

307 *4.1.1. Site 1*

308 The magnetite orebody lies below magnetite-poor (3-6 vol% Mag) serpentized tectonic  
309 harzburgites. The harzburgites show a more or less developed foliation, and are characterized by the  
310 presence of lizardite + antigorite + magnetite  $\pm$  talc pseudomorphs after former olivine and  
311 orthopyroxene (distinguished based on the presence of mesh and bastite textures, respectively) and  
312 relicts of accessory Mg-Al-rich chromite (Table 3). Magnetite is fine-grained ( $<20 \mu\text{m}$ ) and Cr-  
313 bearing (Carbonin et al., 2014). A detailed description of the mineralogy and conditions of  
314 subseafloor serpentization of these rocks was given in Carbonin et al. (2014;  $T = 200\text{-}300^\circ\text{C}$ ,  $\log$   
315  $f_{\text{O}_2} = -36$  to  $-30$ ,  $\log \Sigma S = -2$  to  $-1$ ).

316 Only nodular ores can be found at this site (Fig. 3a, b). Independently of the ore texture, the  
317 gangue mineral assemblage is fairly uniform and comprises, in the order of decreasing abundance,  
318 antigorite, lizardite, forsterite, brucite, clinochlore, carbonates, and Ti-rich chondrodite (Table 3).  
319 Antigorite composes more than 90 vol% of the matrix between the magnetite crystals. It usually  
320 shows an interlocking texture (average grains size =  $150 \mu\text{m}$ ), but it can form euhedral, randomly  
321 oriented blades when in contact with lizardite or magnetite, forming indented crystal boundaries with  
322 the latter mineral (Fig. 4a). This feature was already described in rocks from the western Alps by  
323 Debret et al. (2014), who interpreted it as a prograde dissolution texture produced during Alpine  
324 subduction metamorphism; however, the antigorite studied by Debret et al. (2014) generally has  
325 higher Fe content (up to 8 wt% FeO) than antigorite at Cogne (mostly  $<3$  wt% FeO). Lizardite forms  
326 yellowish aggregates of submicron-sized crystals, which are interstitial between euhedral antigorite  
327 and magnetite. The  $\text{Al}_2\text{O}_3$  content of lizardite ( $\sim 5$  wt%) is systematically higher than that in antigorite  
328 ( $<1$  wt%). Forsterite ( $\text{Fo}_{99}$ ) forms up to  $50 \mu\text{m}$  anhedral crystals, usually arranged into elongated  
329 aggregates, which replace and seldom form pseudomorphs after antigorite. The forsterite crystals are  
330 often altered to fine-grained antigorite along the rim and the fractures. Brucite is of nearly pure Mg-  
331 endmember composition and forms subhedral, tabular crystals up to  $200 \mu\text{m}$  in size. Clinochlore

332 forms tabular crystals and intergrowths with antigorite. These intergrowths probably result from the  
333 breakdown of Al-rich lizardite. The carbonates (calcite, magnesite, dolomite) form anhedral patches  
334 which include antigorite, brucite and fine-grained (<50  $\mu\text{m}$ ) anhedral magnetite. Calcite is the most  
335 common carbonate and is also present as late veins. Ti-rich chondrodite forms up to 500  $\mu\text{m}$ ,  
336 colourless to pale yellow, anhedral crystals, which are sometimes surrounded by a corona of olivine.  
337 Rare accessory minerals are xenotime, sphalerite, Ni-bearing linnaeite, pyrrhotite and uraninite.

338 Magnetite-rich (~25 vol%) diopsidites have also rarely been found. In these peculiar rocks,  
339 magnetite is interstitial between mm- to cm-sized diopside crystals and coexists with antigorite,  
340 andradite and clinocllore. The assemblage antigorite + andradite appears to replace diopside.  
341 Samples of this kind were thoroughly described by Carbonin et al. (2014).

342

#### 343 *4.1.2. Site 2*

344 At this site, the serpentinized tectonic peridotite can be either replaced by fine-grained disseminated  
345 magnetite or crosscut by cm-thick magnetite + chalcopyrite + antigorite veins. The disseminated and  
346 vein ores are deformed and dismembered into lenses by Alpine deformation, which at small scale  
347 results in an anastomosing pattern of mm- to cm-spaced cleavage planes. This deformation is  
348 associated with dynamic recrystallization of antigorite and magnetite, the latter forming elongated  
349 porphyroclasts.

350 The disseminations occur as cm-sized magnetite-enriched bands in antigorite serpentinite and  
351 typically show relict features of the former serpentinized peridotite, i.e., bastites (Fig. 4b) and Mg-  
352 Al-rich chromite grains (Fig. 4c, d; Table 3). The Mg-Al-rich chromite grains (Fig. 4d) are anhedral  
353 and fractured. They are irregularly altered along the rims and fractures into Fe-rich (~41 wt% FeO)  
354 chromite + fine-grained Cr-rich (~4–6 wt%  $\text{Cr}_2\text{O}_3$ , determined by SEM-EDS) chlorite and are  
355 mantled by a continuous rim of Cr-bearing magnetite intergrown with antigorite and minor secondary  
356 diopside.

357 In the vein ores, magnetite forms elongated, millimetric patches with a chalcopyrite core in an  
358 antigorite matrix (Fig. 4e). Magnetite shows well developed crystal boundaries towards chalcopyrite,  
359 while the contacts to the surrounding antigorite are irregular. The limit between the vein and the host  
360 serpentinite is sharp.

361 In both disseminations and veins, antigorite shows an interlocking texture. When it is in contact  
362 to magnetite or lizardite it forms up to 100  $\mu\text{m}$ -long euhedral lamellar crystals, producing typical  
363 indented boundaries. A generation of nearly pure diopside (Table 3) always accompanies magnetite  
364 mineralization. In magnetite disseminations, diopside forms up to 400  $\mu\text{m}$ -long isolated needles,  
365 intergrown with antigorite (Fig. 4c, d), while in the vein ore, it forms rare aggregates of 10-60  $\mu\text{m}$   
366 long crystals disseminated in the vein selvages. From textural relationships, diopside appears to  
367 postdate the formation of bastite pseudomorphs after orthopyroxene in the host serpentinite.

368

#### 369 *4.1.3 Site 3*

370 At this site, the magnetite ores exhibit nodular textures, but only the leopard and massive subtypes  
371 are found. Antigorite is commonly the sole gangue mineral, but the leopard subtype can be  
372 characteristically enriched in diopside  $\pm$  chlorite (Fig. 3d, 4f; Table 3). Antigorite shows an  
373 interlocking texture or forms euhedral crystals when in contact to magnetite or diopside. Antigorite  
374 veins crosscutting diopside crystals have been observed. Diopside has a nearly pure endmember  
375 composition. In the leopard ores, it forms a granofels composed of mm- to cm-sized subhedral  
376 crystals, which include subhedral millimetric magnetite. A late generation of smaller subhedral  
377 crystals ( $<50 \mu\text{m}$ ) fills the interstices between larger grains. The diopside crystals may show patchy  
378 or concentric oscillatory zoning, determined by slight variations in Fe content. Textural relationships  
379 indicate that diopside formed during a late stage of magnetite growth (Fig. 4f), which was then locally  
380 overprinted by antigorite. Veins made up of euhedral diopside in a matrix of lizardite  $\pm$  chlorite are  
381 commonly observed. Clinocllore is found in diopside-rich leopard ores and has variable Mg# ratios  
382 and Al contents (Table 3): the Al-rich variety is found as large (up to 1 mm) subhedral tabular crystals

383 associated with diopside and magnetite; the Al-poor clinochlore is fine-grained and fills the interstices  
384 between larger clinochlore and diopside crystals. Calcite is found as interstitial material between  
385 diopside crystals and as late veins. Rare accessory minerals are andradite, uraninite, talc and apatite.

386

#### 387 *4.1.4. Inclusions in magnetite*

388 The magnetite crystals can be rich in mineral inclusions, which, in the largest poikiloblasts, are  
389 typically concentrated in their cores (Fig. 4a).

390 At Site 1, the most common inclusions are clinochlore and brucite lamellae (Table 3, often  
391 oriented along magnetite (111), anhedral calcite, anhedral sphalerite, rare anhedral pyrite, rare  
392 lizardite and forsterite, and very rare euhedral uraninite and apatite. Antigorite inclusions are often  
393 present in the outermost zones of the magnetite crystals. Composite inclusions made up of clinochlore  
394 + brucite or, rarely, clinochlore + calcite are also observed.

395 At Site 2, the most abundant inclusions are euhedral antigorite and anhedral sulphides. The  
396 sulphides consist of fine lamellar chalcopyrite–cubanite intergrowths and unmixed “bornite solid  
397 solution” grains, composed of lamellar intergrowths of bornite and chalcocite. Also present are  
398 pyrrhotite, which shows exsolution of Co-rich pentlandite, and sphalerite. Other minor included  
399 minerals are lamellar clinochlore and anhedral andradite.

400 At Site 3, the inclusions are mainly composed of clinochlore, which can be associated with rare  
401 andradite (Table 3) and very rare diopside and uraninite; antigorite inclusions are only present near  
402 the rims of the magnetite crystals.

403

404

#### 405 *4.2. Petrography of peculiar host rocks at sites 1 and 3*

406

407 At sites 1 and 3, serpentinites showing a pegmatoid texture are associated with the magnetite ore and  
408 can be variably enriched in magnetite. In the barren rocks (Fig. 3e), cm-sized amoeboid domains



409 made of dominant euhedral coarse-grained (50-300  $\mu\text{m}$ ) antigorite that replaces yellow, fine-grained  
410 (sub-micron sized) lizardite are interweaved with domains composed of mesh textured antigorite +  
411 lizardite and very fine-grained magnetite (magnetite I) lining the rims of the mesh. Lizardite is Al-  
412 rich in both domains (Raman peak at 382-385  $\text{cm}^{-1}$ , indicating Al substitution for Si in the tetrahedral  
413 sites; Groppo et al., 2006). Coronae of interlocking antigorite line the boundaries between the two  
414 domains. In magnetite-enriched rocks, the early fine-grained ( $<30 \mu\text{m}$ ), usually euhedral magnetite  
415 (I) associated with Al-rich lizardite (Table 3) is overgrown by a new generation of coarser-grained,  
416 subhedral to anhedral disseminated magnetite (magnetite II) + euhedral antigorite + lamellar  
417 clinocllore. Clinocllore probably forms as consequence of the transformation of Al-rich lizardite to  
418 Al-poor antigorite, since its content is proportional to the amount of antigorite that replaces lizardite.  
419 The two magnetite generations have similar major element compositions (Table 3). Possible  
420 variations in trace element compositions could not be determined because of the small crystal size of  
421 magnetite I. Magnetite II can completely replace the lizardite-rich domains, but the amoeboid shape  
422 of the domains and the antigorite coronae are usually preserved (Fig. 3f, Fig. 4g, h). On the contrary,  
423 the antigorite domains and coronae show only scarce anhedral magnetite (Fig. 4g, h). A magnetite-  
424 rich diopsidite, composed of dominant fine-grained diopside ( $<50 \mu\text{m}$ ), subordinate magnetite and  
425 minor euhedral antigorite ( $<150 \mu\text{m}$ ; Fig. 3f; Tables 3 and 4), has been observed in contact with the  
426 magnetite-rich pegmatoid serpentinite.

427

428

#### 429 *4.3. Bulk rock geochemistry*

430

431 Bulk rock compositions are reported in Table 4. The magnetite-poor ( $\text{Fe}_2\text{O}_3 < 8.5 \text{ wt}\%$ ) serpentinitized  
432 peridotites have major and trace element concentrations typical for refractory peridotites (cf.  
433 Andreani et al., 2014; Bodinier and Godard, 2003; Niu, 2004; Paulick et al., 2006), such as low  $\text{Al}_2\text{O}_3$   
434 ( $\sim 1\text{-}3 \text{ wt}\%$ ) and  $\text{TiO}_2$  (0.02-0.1 wt%), high Ni ( $\sim 1400\text{-}2800 \text{ ppm}$ ) and Cr ( $\sim 1900\text{-}2600 \text{ ppm}$ ) and low

435 Co/Ni ratio (~0.05-0.07). The Cu and Zn contents (~20 and ~40-50 ppm, respectively) are also typical  
436 for upper mantle peridotites (cf. O'Neill and Palme, 1998; Niu 2004; Fouquet et al. 2010). The  
437 pegmatoid serpentinites have variable Al<sub>2</sub>O<sub>3</sub> (~0.8-2.6 wt%), Fe<sub>2</sub>O<sub>3</sub> (~4.5-10 wt%), Ni (~500-2000  
438 ppm), and Cr (~10-2700 ppm) contents and Co/Ni ratios (~0.05-0.2). However, Cu and Zn show very  
439 little variation (~20 and ~30-40 ppm, respectively).

440 The magnetite-enriched (Fe<sub>2</sub>O<sub>3</sub> >28 wt%) serpentinites have different compositions reflecting  
441 their distinct host rocks. The magnetite-rich pegmatoid serpentinite has a high Al<sub>2</sub>O<sub>3</sub> content (~2  
442 wt%) and a high Co/Ni ratio (~0.4), but low Ni, Cr, Cu and Zn contents (~280, ~10, ~70, ~60 ppm,  
443 respectively). The fine-grained disseminated ore has Al<sub>2</sub>O<sub>3</sub>, Cr and Ni contents (~1 wt%, ~2200,  
444 ~1200 ppm, respectively) in the same range as the magnetite-poor serpentinitized peridotites, but has  
445 higher Cu and Zn contents (~200 and ~120 ppm, respectively) and a higher Co/Ni ratio (~0.1). With  
446 further increase in magnetite content, the concentrations of Cr (~1300 ppm) and Ni (~240 ppm)  
447 decrease, but the Co/Ni ratio increases (~0.6). The magnetite vein ore (Fe<sub>2</sub>O<sub>3</sub> ~44 wt%) has low Ni  
448 (~500 ppm) and Cr (~70 ppm) contents and an intermediate Co/Ni ratio (~0.3). Moreover, it exhibits  
449 moderately high Zn (130 ppm) and the highest Cu content (~14000 ppm), which reflects the presence  
450 of chalcopyrite. The magnetite-rich diopsidite (Fe<sub>2</sub>O<sub>3</sub> ~21 wt%) has a trace element composition  
451 similar to that of the pegmatoid serpentinite it is in contact with, but it has a higher Co/Ni ratio (~0.9).

452 In the nodular ores, the SiO<sub>2</sub> and MgO contents are inversely proportional to the amount of  
453 magnetite present. The Al<sub>2</sub>O<sub>3</sub> and CaO concentrations are variable and reflect the different relative  
454 abundances of clinocllore and diopside (or carbonates), respectively. The TiO<sub>2</sub> content is generally  
455 low (0.02 wt%), but in the ore from Site 1 it can be slightly higher (~ 0.06 wt%), consistently with  
456 the presence of Ti-rich chondrodite. The nodular ores are virtually Cr-free (~10 ppm), have low Ni  
457 (~10-110 ppm) and relatively high Co (~320-440 ppm) contents, which translate into the highest  
458 observed Co/Ni ratios (~3-30). Moreover, compared to serpentinitized peridotites and pegmatoid  
459 serpentinites, they show somewhat higher Cu and Zn (~30-50 ppm and ~80-100 ppm, respectively).  
460 The nodular ores, the magnetite-rich pegmatoid serpentinite and the magnetite-rich diopsidite share

461 significant U and Th contents, which reach the maximum values at Site 1 (U = 2.9 ppm; Th = 0.9  
462 ppm). In both magnetite-poor and magnetite-enriched serpentinized tectonic peridotites, U and Th  
463 contents are below the detection limits of ICP-MS analysis (<0.01 and <0.02 ppm, respectively).

464 The relationships between magnetite enrichment, Co/Ni ratio and Cr content are shown in Figure  
465 5. Magnetite enrichment is generally accompanied by an increase in the Co/Ni ratio, but shows no  
466 correlation with the Cr content. In particular, the Cr content is very low (<30 ppm) in the nodular  
467 ores, in the diopsidites and in most pegmatoid serpentinites (both magnetite-poor and magnetite-  
468 enriched) and is higher (Cr >1200 ppm) in both barren and magnetite-enriched serpentinites after  
469 peridotites.

470

471

#### 472 *4.4. Age of the deposit*

473

474 The high U (+ Th) contents in nodular ores from Site 1 and Site 3 can be attributed to the presence of  
475 uraninite inclusions in magnetite. Uraninite forms anhedral to euhedral cuboctahedral crystals,  
476 ranging in size from ~1 to 40  $\mu\text{m}$  (Fig. 6a-c, e, g). Textural evidence suggests that uraninite and  
477 magnetite (+clinocllore) were contemporaneous (Fig. 6b, g). The compositions of the uraninite  
478 crystals are reported in Table 5. The U/Th ratios are variable (3 to 21), especially at Site 1, where  
479 both the highest and the lowest Th contents were measured. The FeO and CaO concentrations are  
480 relatively high (FeO = 0.8-4.9 wt%; CaO = 0.06-1.2 wt%), but they are unrelated to PbO contents,  
481 which excludes late-stage alteration (Alexandre and Kyser, 2005). Excitation of the host magnetite  
482 within the microprobe interaction volume could explain the presence of Fe in the analyses. On the  
483 contrary, the Ca content is considered to be primary and ascribed to lattice-bound substitutions of Ca  
484 for U. A less than 1  $\mu\text{m}$ -thick, U-rich rim is sometimes observed in uraninite crystals (Fig. 6e), and  
485 is ascribed to partial alteration.

486 The U-Th-Pb ages calculated for a group of three small (<10  $\mu\text{m}$ ) uraninite grains from Site 1  
487 (Fig. 6a-c) are plotted in Fig. 6d. Due to the small grain size, only single-spot analyses were acquired.  
488 The weighted average age is  $161.8 \pm 3.5$  Ma (MSWD = 0.51). Figure 6f shows the ages obtained for  
489 an aggregate of zoned grains from Site 1 (Fig. 6e). The crystals have a U-rich rim, which testifies for  
490 partial alteration. Therefore, we only considered sixteen analyses that form a plateau for PbO, UO<sub>2</sub>  
491 and ThO<sub>2</sub> concentrations (Fig. 7). The weighted average age for the plateau, after rejecting two  
492 outliers, is  $150.8 \pm 2.0$  Ma (MSWD = 1.03). The weighted average age calculated for a big ( $\sim 40$   $\mu\text{m}$ ),  
493 unzoned uraninite crystal from Site 3 (Fig. 6g), which is intergrown with magnetite and contains  
494 chlorite, is  $151.9 \pm 1.4$  Ma (MSWD = 0.91) (Fig. 6h). Also in this case only plateau PbO values were  
495 considered (Fig. 7). The two age determinations that yield the lowest uncertainties and best MSWD  
496 values (i.e., close to unity) are within errors of each other and are considered to be the most reliable.  
497 However, considering the limited age scatter, it is reasonable to combine all the data into a single age  
498 determination, which yields a value of  $152.8 \pm 1.3$  Ma (MSWD = 1.3; Fig 6i).

499

500

#### 501 *4.5. Geochemistry of Cogne magnetite*

502

503 The compositions of the Cogne magnetites are reported in Tables 3 and 6. The magnetites show  
504 significant substitutions of Fe by Mg and Mn (Fig. 8). The concentrations of these metals are the  
505 highest at Site 1 (median =  $\sim 24100$  ppm and  $\sim 5000$  ppm, respectively). Concentrations of Ca, Si, Mo,  
506 Zr and Cr are generally below or close to the ICP-MS detection limits; only magnetite forming the  
507 disseminated ore from Site 2 has significant Cr contents, which can be as high as  $\sim 150$  ppm. Among  
508 the other trace elements, the concentrations of Ni, Co, Ti, and Zn are generally an order of magnitude  
509 higher than those of V (Fig. 8). The highest concentrations of Co are found at Site 1 (median =  $\sim 570$   
510 ppm), whereas the lowest concentrations are in magnetite in disseminated ore from Site 2 (median =  
511  $\sim 80$  ppm). In spite of across-site variations, the Co content is fairly constant in magnetite from the

512 same sample. The Ti content is the highest in magnetite from disseminated ore from Site 2 (median  
513 = ~570 ppm) and the lowest in magnetite from diopside-rich rocks from Site 1 and Site 3 (median =  
514 ~60 ppm). The Ni and V contents are highest in magnetite from the magnetite-rich pegmatoid  
515 serpentinite (median = ~670 ppm and ~60 ppm, respectively). The lowest Ni and V contents are  
516 observed in Site 1 ore (median = ~80 ppm) and in vein magnetite (median = ~6 ppm), although in the  
517 latter both elements are highly variable. The Zn contents show minor variability: the highest values  
518 are found in the vein magnetite (median: ~160 ppm) and the minimum values are found in magnetite  
519 from Site 3 (median: ~80 ppm).

520 Robust PCA indicates that the two first principal components (PC1 and PC2) can explain 97%  
521 of the variability of the magnetite compositional data and thus can adequately be used to describe the  
522 various magnetite populations. As shown by the loading plot (Fig. 9), Mg, Mn, Co and Zn are highly  
523 correlated, while Ni is anti-correlated and V and Ti vary independently from the other elements. In  
524 the PC1 vs. PC2 plot, one cluster of samples, which encompasses the magnetites in the nodular ores  
525 from Site 1 and Site 3 and the magnetite-rich diopside, is characterized by the highest (Mg, Mn, Co,  
526 Zn)/Ni ratios. High Ni contents are instead distinctive of disseminated magnetite in serpentinitized  
527 peridotite and in the magnetite-rich pegmatoid serpentinite from Site 3 (Fig. 8). These high-Ni  
528 magnetites form two distinct groups, in which high Ni is associated with high Ti (and Cr) and high  
529 V, respectively. Vein magnetites, having a very variable Ni and low overall V, plot in an intermediate  
530 position between high-Ni and low-Ni magnetites. When plotted on the Zn vs. Co plane (Fig. 10),  
531 most of the magnetites show a nearly constant Zn/Co ratio of ~0.28. Magnetites in the veins and in  
532 the fine-grained disseminated ore have higher Zn/Co ratios (~1).

533

534

535 *4.6. Thermodynamic modelling*

536

537 We attempted to reproduce the mineral assemblages observed at Cogne in a model seafloor  
538 hydrothermal system. The fluids produced by interaction at 400°C of modified seawater with  
539 harzburgite and Fe-gabbro (Table 2), respectively, provide two potential endmember compositions  
540 for fluids circulating in and reacting with the original oceanic substrate rocks. Harzburgite composes  
541 the uppermost part of the Cogne deposit and is the most common type of abyssal peridotite (Mével,  
542 2003). Fe-gabbro is the most Fe-rich rock that can be found in the ophiolitic units of southern Valle  
543 d'Aosta (Benciolini et al., 1988; Bocchio et al., 2000; Dal Piaz et al., 2010; Polino et al., 2014) and  
544 it can be an efficient source of iron if altered at high temperature. Based on our calculations, dissolved  
545 Fe in the harzburgite-reacted fluid (Fig. 11a) increases from W/R ~1 to W/R ~7 where it reaches a  
546 maximum value of ~11 mmol/kg (604 ppm). The increase in Fe concentration follows the pH  
547 decrease that is in turn controlled by hydrolysis of mantle orthopyroxene, which is much more  
548 reactive than olivine at 400°C (Charlou et al. 2002). In general, the Fe-gabbro-reacted fluids are more  
549 acidic and more Fe-rich. The Fe concentration is up to one order of magnitude higher (Fig. 11b),  
550 reaching a maximum value of ~26 mmol/kg (1439 ppm) at W/R ~80. Such a high dissolved Fe content  
551 again reflects a pH minimum, which immediately follows the total breakdown of plagioclase. This is  
552 consistent with experimental evidence that plagioclase alteration to Mg-silicates (chlorite, epidote,  
553 talc) by seawater at 400°C and high W/R buffers pH to low values (Seyfried, 1987; Seyfried et al.,  
554 2010). Other major differences between the two fluid types at their Fe peak concern the  
555 concentrations of Mg and Si, which are about one order of magnitude lower and two order of  
556 magnitude higher, respectively, in the Fe-gabbro-reacted fluid. The high W/R ratios required to  
557 maximize the Fe contents could potentially be achieved in a highly fractured substrate, such as at the  
558 foot wall of a detachment fault in an oceanic core complex (e.g., McCaig et al., 2007).

559 The harzburgite-reacted and Fe-gabbro-reacted fluids carrying the maximum dissolved Fe were  
560 further reacted at either 300°C or 400°C with the different lithologies listed in Table 2. We considered  
561 temperatures  $\geq 300^\circ\text{C}$  to account for the ubiquitous presence of antigorite (predominant at  $T > 300^\circ\text{C}$ ;  
562 Evans, 2004, 2010) in all ore assemblages at Cogne and because these high temperatures disfavour

563 substitution of Fe for Mg in minerals (especially in brucite; Klein et al., 2009), thus accounting for  
564 the very high  $100 \cdot \text{Mg}/(\text{Mg}+\text{Fe})_{\text{mol}}$  ratios ( $\text{Mg}\# >90$ ) of gangue minerals in the Cogne deposit (Table  
565 3). Moreover, at the high temperatures considered, and especially at high W/R ratios, the  
566 thermodynamic properties of the very Mg-rich gangue minerals are well approximated by their Mg  
567 endmembers, hence neglecting solid solutions can be considered to be a minor problem. The only  
568 mineral phase that significantly deviates from the ideal composition is lizardite, which is always Al-  
569 rich (Table 3). However, textural evidence indicates that lizardite is a minor relict phase that was  
570 formed during an early serpentinization event and rarely survived the successive higher temperature  
571 ore-forming process (cf. section 4.1). Accounting for the presence of Al-rich lizardite would not have  
572 significantly influenced the modelling of the fluid-rock system at high temperature.

573 The mineral assemblages produced by hydrothermal fluid-rock interactions are shown in Figure  
574 12. Magnetite is stable for both fluids over the whole considered W/R range at both 300°C and 400°C  
575 (with the exception of fresh troctolites reacting with harzburgite-reacted fluid at 300°C). Under *rock-*  
576 *dominated conditions* ( $W/R < 1$ ), the final alteration mineral assemblages are similar for both fluids:  
577 forsterite and brucite are generally formed in addition to magnetite, but their stability is dependent on  
578 temperature, with forsterite being stable at higher temperature (Fig. 12b, d) than brucite (Fig. 12a, c).  
579 Fayalite is predicted to form at both 300°C and 400°C in fresh troctolites and pegmatoid serpentinites.  
580 The presence of pure fayalite may be an artefact induced by neglecting solid solutions in olivine.  
581 Clinocllore is present in all mineral assemblages at 400°C (with the exception of the model of a fresh  
582 dunite reacting with harzburgite-reacted fluid), but at 300°C it forms in abundant quantities only in  
583 troctolites (both fresh and serpentinized) and pegmatoid serpentinites. Diopside is abundant only in  
584 Ca-rich rocks, i.e. harzburgites and troctolites (Table 2), and in troctolites it is associated with  
585 tremolite. In these rocks also minor anhydrite forms. At 300°C in fresh harzburgites and serpentinized  
586 dunites the diopside is soon destabilized and the liberated Mg and Si combine with dissolved Al to  
587 form clinocllore. At higher temperatures this reaction is limited to higher W/R ratios. Some  
588 phlogopite is produced during alteration of fresh troctolites. At *intermediate W/R ratios*, diopside

589 disappears at both 300°C and 400°C. In troctolites, diopside breakdown is accompanied by an  
590 increase in the modal amount of tremolite (and fayalite at 300°C). In serpentinized harzburgites,  
591 diopside reacts at 300°C with brucite and magnetite to form andradite and antigorite (cf. reaction n.  
592 44 in Frost and Beard, 2007; Fig. 12a, c). Talc becomes abundant in pegmatoid serpentinites at 400°C,  
593 but at 300°C it only forms when the rocks react with Fe-gabbro derived fluid. Formation of talc is  
594 enhanced by the low pH, high Si and low Ca activities of the Fe-gabbro-reacted hydrothermal fluid.  
595 *At high W/R ratios*, in both fresh and serpentinized dunites and harzburgites, brucite reacts with either  
596 the harzburgite-reacted fluid or the Fe-gabbro reacted fluid to form antigorite or clinochlore,  
597 respectively. Talc is formed in Si-rich systems, i.e. those involving Si-rich lithologies (troctolites,  
598 pegmatoid serpentinite) or fluids (Fe-gabbro-reacted fluids). In the systems dominated by Fe-gabbro-  
599 reacted fluids, talc replaces forsterite and antigorite, thus forming talc + magnetite + clinochlore  
600 assemblages.

601

## 602 **5. Discussion**

603

### 604 *5.1. Cogne as an ultramafic-hosted subseafloor hydrothermal deposit*

605

#### 606 *5.1.1. Constraints from magnetite geochemistry and ocean seafloor studies*

607 Important clues about the origin of the Cogne magnetite can be derived from the comparison with  
608 existing published datasets for magnetite from various genetic environments. The Cogne magnetite  
609 is poor in Ti and Cr (<640 ppm and <150 ppm, respectively), which is a typical feature for  
610 hydrothermal magnetite (Fig. 13). In fact, based on the data compiled by Dare et al. (2014),  
611 hydrothermal magnetite can be distinguished from magmatic magnetite, because the former has  
612 generally low Ti contents (<10000 ppm) and high Ni/Cr ratios ( $\geq 1$ ), in virtue of the higher mobility  
613 of Ni in aqueous fluids. Cogne magnetite is also poor in V (<140 ppm) and rich in Mn (>2500 ppm),  
614 similar to hydrothermal magnetite from skarn deposits (Fig. 14). However, the Cogne magnetite ore



615 was not emplaced in carbonate rocks but in mantle serpentinites, as testified by the geochemical and  
616 textural features of the host rocks.

617         Serpentinization of peridotites can produce magnetite that is depleted in Cr, Ti, V and Ni  
618 compared to the primary magmatic magnetite (Boutroy et al., 2014). However, serpentinization alone  
619 cannot account for the amount of magnetite observed in most of Cogne rocks. In fact, magnetite  
620 production during serpentinization is limited by the amount of FeO available in the peridotite, which  
621 is commonly less than 10 wt% (Bodinier and Godard, 2003). Therefore, an efficient mechanism of  
622 mobilization and concentration of Fe is needed to explain the formation of the Cogne deposit.

623         Low-T (100-300°C) hydrothermal fluids causing peridotite serpentinization at high W/R can  
624 leach Fe from the peridotite and precipitate it as magnetite in veins (up to a few cm-thick), as reported  
625 for the Bou Azzer ophiolite, Morocco (Gahlan et al., 2006). However, the compositions of Bou Azzer  
626 vein magnetites, although considerably depleted in trace elements as a consequence of their low  
627 formation temperatures (Nadoll and Koenig, 2011), are very different from those of Cogne  
628 magnetites. The latter have higher Co/Ni ratios (0.2-67 vs. 0.004-0.12) and are richer in Mn (2600-  
629 5000 vs. 400-470 ppm), Zn (80-160 vs. 3-20 ppm) and Mg (5600-24000 vs. 97-1000 ppm). These  
630 differences suggest that the formation of Cogne magnetite took place under substantially dissimilar  
631 physicochemical conditions.

632         Some indications on the various factors that controlled the composition of Cogne magnetite  
633 can be derived from the PCA (Fig. 9). The PC1 clearly discriminates high-(Mg, Mn, Co, Zn)  
634 magnetites in nodular ores and diopsidites from high-(Ni, V, Ti) magnetites in fine-grained  
635 disseminated ore and in magnetite-rich pegmatoid serpentinite. The relatively low Mn, Co and Zn  
636 contents in the host rocks and the fluid-compatible nature of these metals suggests that the  
637 composition of the high-(Mg, Mn, Co, Zn) magnetites was controlled by an externally-buffered fluid  
638 (cf. Dare et al., 2014; Nadoll et al., 2014). The high Co/Ni ratios these magnetites (Table 6) also  
639 support this hypothesis, because it would suggest a mafic metal source (cf. Melekestseva et al., 2013),  
640 which is in contrast with the ultramafic nature of most of the Cogne host rocks. On the contrary, the

641 high-(Ni, V, Ti) magnetites are more enriched in elements that are weakly mobile and/or relatively  
642 abundant in the host rocks, suggesting formation under rock-buffered conditions (cf. Nadoll et al.,  
643 2014). The PC1 may thus be interpreted as reflecting magnetite formation under different W/R ratios  
644 from possibly similar parent fluids. The PC2 further discriminates between the different host rocks  
645 (i.e. high-V magnetite in pegmatoid serpentinite and high-Ti magnetite in serpentinitized tectonic  
646 peridotites). Magnetite in veins shows intermediate geochemical features between hydrothermal  
647 fluid-buffered and host rock-affected compositions.

648 Hydrothermal fluids carrying a significant load of transition metals (high Fe, Mn, Cu, Zn  $\pm$   
649 Co  $\pm$  Ni) issue from ultramafic substrates in high-T (>350°C) hydrothermal systems associated with  
650 oceanic core complexes in slow-spreading mid-oceanic ridges, such as at Rainbow and Logatchev on  
651 the Mid-Atlantic Ridge (Douville et al. 2002; Andreani et al., 2014). In particular, the hydrothermal  
652 vent fluids at Rainbow are the richest in Co (Douville et al., 2002), have the highest Co/Ni ratios ( $\sim$ 4)  
653 and are probably saturated in magnetite + chlorite + talc (Seyfried et al., 2011). The surveyed portion  
654 of the Rainbow hydrothermal deposit is almost entirely made up of sulphides (Fouquet et al., 2010;  
655 Marques et al., 2006, 2007), as expected for the upper part of a seafloor hydrothermal system, where  
656 the hot hydrothermal fluid mixes with seawater (Janecky and Seyfried, 1984). Notwithstanding this,  
657 at Rainbow, hydrothermal magnetite is locally abundant in serpentinites hosting sulphide stockworks  
658 and in semi-massive sulphides, where magnetite sometimes replaces pyrite (Marques, 2005).  
659 Magnetite forming coarse-grained disseminations in the serpentinites that host stockworks at  
660 Rainbow precipitated later than the sulphides during a distinct hydrothermal stage (Marques et al.,  
661 2006) and, notably, has a similar geochemical fingerprint as magnetite in fine-grained disseminations  
662 in serpentinitized peridotites at Cogne (the concentrations of the trace elements, with the exception of  
663 Si, are in the same order of magnitude). Recently, Yıldırım et al. (2016) described a hydrothermal  
664 magnetite mineralization in a non-metamorphic volcanogenic massive-sulphide (VMS) deposit from  
665 the Upper Triassic-Upper Cretaceous Koçali complex, a Tethyan ophiolite in Turkey. These findings  
666 and the above observations support the possibility that Cogne magnetite has directly formed in a

667 seafloor hydrothermal system. The presence of a positive magnetic anomaly at Rainbow has been  
668 ascribed to a  $\sim 2 \cdot 10^6 \text{ m}^3$  magnetite-rich stockwork zone (Szitkar et al., 2014). If this volume was  
669 entirely composed of magnetite, it would correspond to 10 Mt of mineral, which is on the same order  
670 of magnitude as the estimated amount of magnetite at Cogne ( $\sim 12$  Mt). It is worth noting that the  
671 Rainbow hydrothermal system is still highly active (Fouquet et al. 2010) and its vent fluids are  
672 magnetite-saturated (Seyfried et al., 2011). It can thus be inferred that the Rainbow hydrothermal  
673 system may eventually produce at depth a magnetite deposit of comparable size as Cogne.

674 In such a scenario, the general scarcity of sulphides at Cogne, along with their presence in the  
675 veins above the main magnetite bodies, suggest that the exposed mineralized section represents the  
676 deep segment of a seafloor, ultramafic-hosted, high-temperature hydrothermal system, which was  
677 possibly associated with shallower, now eroded, sulphide-rich bodies. According to this  
678 interpretation, the magnetite + sulphide veins and fine-grained disseminations in the hanging wall  
679 serpentinite (Site 2) may mark the transition between the magnetite-rich and the sulphide-rich  
680 portions of the hydrothermal system (Fig. 15).

681

#### 682 *5.1.2. Geological, geochronological and textural constraints*

683 The Cogne mantle peridotites underwent complete serpentinization at 200-300°C beneath the seafloor  
684 of the Jurassic Piedmont-Liguria ocean (Carbonin et al., 2014). Our radiometric data on magnetite-  
685 associated uraninite ( $152.8 \pm 1.3$  Ma) places the ore-forming event in proximity of the Kimmeridgian-  
686 Tithonian boundary ( $152.1 \pm 0.9$  Ma). This age overlaps with that of the spreading of the Piedmont-  
687 Liguria ocean, as inferred by biochronological dating of supra-ophiolitic deep-sea sediments  
688 (radiolarites), whose oldest ages span from Late Bajocian to Middle Bathonian ( $\sim 168$  Ma; Cordey et  
689 al., 2012), and by radiometric dating of magmatic rocks, which places the latest magma pulses  
690 (mainly plagiogranites) in the Western Alps and Liguria in the Kimmeridgian-Tithonian ( $\sim 157.3 \pm$   
691  $1.0 - \sim 145.5$  Ma; Lombardo et al., 2002; Manatschal and Müntener, 2009 and references therein).

692           Very little information can be obtained about the original lithological and thermal structure of  
693 the oceanic lithosphere at Cogne, because of the limited exposure. Some indirect information can be  
694 obtained from the nearby Mt. Avic serpentinite massif (Fig. 1). Although located in a different  
695 structural position in the orogen (see Dal Piaz et al., 2010), the Mt. Avic massif provides the most  
696 complete section of the oceanic lithosphere of the Alpine Tethys in the southern Valle d'Aosta region.  
697 In the Mt. Avic massif, dominant serpentinitized mantle peridotites, associated with gabbroic  
698 intrusions (Mg-metagabbros), rodingitic dykes, minor Fe-Ti-oxide metagabbros and other  
699 metabasites (Dal Piaz et al., 2010; Fontana et al. 2008, 2015; Panseri et al., 2008), are thought to have  
700 been exposed on the seafloor in an oceanic core complex (Tartarotti et al., 2015). This is consistent  
701 with the proposed slow- to ultra-slow nature of the Piedmont-Liguria ocean (Manatschal et al., 2011;  
702 Manatschal and Müntener, 2009; Piccardo et al., 2008). Jurassic magmatic activity in the Mt. Avic  
703 massif was sufficient to sustain high-temperature hydrothermal convection cells, as testified by  
704 widespread, small, massive sulphide (Cu-Fe-Zn) deposits, which are mostly associated with  
705 metabasites (Castello et al., 1980; Castello, 1981; Martin et al., 2008; Dal Piaz et al., 2010; Fantone  
706 et al., 2014) and are thought to have formed in the seafloor (Martin et al., 2008). The distinctive  
707 enrichment in Co and Cu observed in Cogne nodular and vein magnetite ores, respectively, as well  
708 as the low Ni content in all magnetite ore types, suggests a contribution from mafic sources or a  
709 combined contribution from ultramafic and mafic sources, as observed in some ultramafic-hosted,  
710 mid-ocean ridge, hydrothermal deposits (e.g. Rainbow, Fouquet et al., 2010; Marques et al., 2006;  
711 Semenov, Melekestseva et al., 2014) and in other ultramafic-hosted VMS deposits in ophiolitic belts  
712 (Melekestseva et al., 2013). In analogy with these modern and ancient examples, also at Cogne the  
713 presence of deep magmatic intrusions (gabbro) would be required to provide heat and suitable  
714 chemical conditions (low pH) to produce metal-rich fluids (e.g., Marques et al., 2006; Seyfried et al.,  
715 2011). Gabbroic intrusions, mainly represented by gabbros and Fe-Ti gabbros, are not observed in  
716 the small Cogne unit, but are common in the wider Mt. Avic area (see above) and in the other  
717 ophiolitic units in southern Valle d'Aosta (Grivola-Urtier and Zermatt-Saas units; Benciolini et al.,

718 1988; Bocchio et al., 2000; Dal Piaz et al., 2010; Polino et al., 2014). Therefore, we infer that similar  
719 rock types could have occurred also at Cogne in the original oceanic lithosphere section.

720 The texture, geochemistry (low Co/Ni, high Cr) and relict mineralogy (bastites, Mg-Al-rich  
721 chromite) of Site 2 magnetite-enriched serpentinites suggest that the host rock was a harzburgitic  
722 mantle tectonite, with composition comparable with that of modern abyssal peridotites. However,  
723 chemical and textural evidence from both Site 1 and Site 3 indicates that part of the hydrothermal ore  
724 was emplaced in more atypical serpentinites, which exhibit a ghost pegmatoid texture marked by  
725 interlobate domains separated by coronae structures (Fig. 3f). Similar textures have been described  
726 in some troctolites from modern oceanic and ancient ophiolitic settings (Blackman et al., 2006; Renna  
727 and Tribuzio, 2011). These rocks are interpreted to have formed from melt-impregnation and melt-  
728 peridotite reactions, which dissolved orthopyroxene and partially dissolved olivine producing  
729 rounded or embayed grain boundaries (Drouin et al., 2009; Renna and Tribuzio, 2011; Suhr et al.,  
730 2008). In particular, olivine-rich troctolites originating from melt-peridotite reactions are usually  
731 coarse-grained and can show a harrisitic texture (Renna and Tribuzio, 2011), which is reminiscent of  
732 the “harrisitic” texture of some nodular ores at Cogne. This suggests that many, if not most, nodular  
733 ores at Cogne formed by hydrothermal alteration of original serpentinitized troctolites, with magnetite  
734 preferentially replacing the original olivine domains.

735

### 736 *5.1.3. Insights from thermodynamic modelling*

737 From a qualitative point of view, interaction of various types of fresh or serpentinitized mantle rocks  
738 with either a harzburgite-reacted fluid at intermediate to high W/R or a Fe-gabbro-reacted  
739 hydrothermal fluid at intermediate W/R (Fig. 12) can produce mineral assemblages made of  
740 magnetite + antigorite + clinocllore ± brucite (at 300°C) ± forsterite (at 400°C), which resemble the  
741 most common mineral assemblages in the Cogne magnetite ores. However, even when the natural  
742 mineral assemblage is qualitatively reproduced, the calculated modal magnetite content invariably  
743 remains too low to produce a magnetite ore. This indicates that our model fluids are not sufficiently

744 Fe-rich to account for the formation of the Cogne deposit. Note that a Rainbow-type fluid (Table 7)  
745 would produce broadly similar mineral assemblages as our model fluids, since its Na, Mg, Si, Fe, Cl  
746 concentrations are fairly similar. We could not envisage any other reasonable substrate lithology  
747 which could have released significantly higher Fe to the hydrothermal fluids under reasonable  
748 conditions. This suggests that additional processes other than simple seawater/rock reactions have  
749 played a role in the formation of the magnetite parent fluids.

750 One such process could be phase separation in the hydrothermal fluid, which could have  
751 produced brines enriched in weakly volatile Fe. Phase separation is commonly invoked to explain the  
752 wide chlorinity range observed in modern seafloor hydrothermal vent fluids (e.g., Bischoff and  
753 Rosenbauer, 1987; Charlou et al., 2002; Douville et al., 2002; Foustoukos and Seyfried, 2007; Pester  
754 et al., 2014; Seyfried et al., 2011). A higher chlorinity would enhance solubility of metals as chloride  
755 complexes. At the same time, H<sub>2</sub>S partitioning into the vapour phase would cause sulphide  
756 undersaturation in the brine (Bischoff and Rosenbauer, 1987; Fouquet et al., 2010; Seyfried et al.,  
757 2004; Seyfried et al., 2010; Von Damm, 2004), thus delaying sulphide precipitation. This is in  
758 agreement with the general scarcity of sulphides in the Cogne magnetite ores. The presence of  
759 chalcophile metals in the fluid is still testified by Cu sulphides in magnetite veins from Site 2. In this  
760 case, the transition from bornite + magnetite to chalcopyrite + magnetite assemblages suggests a  
761 progressive variation in the parent fluids towards higher H<sub>2</sub>S activity or lower Cu/Fe ratios (cf.  
762 Seyfried et al., 2004, 2010).

763 Another process which could potentially lead to enhanced Fe concentrations in the fluid is the  
764 incorporation of a magmatic gaseous component, which could promote acidification and thus increase  
765 Fe solubility (cf. Berkenbosch et al., 2012; de Ronde et al., 2011). However, assuming a gas  
766 composition similar to that of gases emitted from mafic lavas (Erta 'Ale volcano, Ethiopia; Sawyer et  
767 al., 2008), it can be calculated that a relatively high condensed gas/fluid mass ratio of 1:10 would  
768 increase the Fe concentrations only by a factor of ~2.3. This increase is too small to allow a significant

769 increase in the final amount of precipitated magnetite. Therefore, phase separation remains the most  
770 likely hypothesis.

771 Another feature that is not explained by our models is the diopside-rich gangue observed at  
772 Site 3. Textural relationships suggest that diopside formed during a late stage of magnetite  
773 mineralization, most likely from a fluid with higher pH and/or higher  $\text{Ca}^{2+}$  activity (see Fig. 9 in Bach  
774 and Klein, 2009). This fluid could have derived from serpentinization of country peridotites and  
775 troctolites, and may thus have some affinity with rodingite-forming fluids. Alternatively, a higher Ca  
776 content could result from more extensive interaction with gabbroic rocks. The possible role of  
777 gabbroic rocks in producing Ca-Si-(Al)-rich fluids has been suggested, for instance, for fluids  
778 responsible for strong calcic metasomatism in fault zones in modern oceanic core complexes (Boschi  
779 et al., 2006).

780

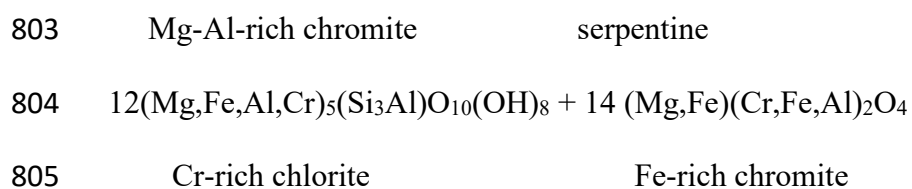
781

## 782 *5.2. Alternative hypotheses*

783

784 As ultramafic rocks in ophiolitic massifs often contain accumulations of chromite (e.g., Bédard and  
785 Hébert, 1998), a potential origin of magnetite in Sites 1 and 3 could be by leaching of Cr from former  
786 chromitite bodies. Indeed, Cr appears to be mobile during high-temperature ( $>500\text{-}550^\circ\text{C}$ ) peridotite-  
787 water interactions, as shown by Arai and Akizawa (2014) for the Oman ophiolite. Also, in the Mt.  
788 Avic massif, some small-scale magnetite ores were apparently formed after former chromitites  
789 (Diella et al., 1994; Rossetti et al., 2009). There are two lines of evidence against this hypothesis for  
790 the Cogne magnetite. First, in the Mt. Avic ores, chromite is still preserved in the cores of the  
791 magnetite grains (Diella et al., 1994; Fontana et al., 2008; Rossetti et al., 2009), whereas neither  
792 chromite relicts nor Cr-rich magnetite cores are found in nodular and vein ores at Cogne. Second,  
793 there is no evidence for a high-temperature alteration at Cogne such as that described in the Oman  
794 ophiolite by Arai and Akizawa (2014). At the temperatures under which serpentinization and

795 successive hydrothermal metasomatism at Cogne took place (200-300°C and 300°-400°C,  
 796 respectively; Carbonin et al., 2014), Cr is essentially immobile and any Cr dissolved at higher  
 797 temperatures deeper in the system should be precipitated (Arai and Akizawa, 2014). The immobility  
 798 of Cr during magnetite mineralization is testified by the mantle tectonites containing the fine-grained  
 799 disseminated magnetite from Site 2, which have similar bulk-rock Cr content as their magnetite-poor  
 800 counterparts (Fig 5). In these rocks, the original Mg-Al-rich chromite (the main Cr carrier) was  
 801 replaced *with no Cr loss* by Fe-rich chromite + Cr-rich chlorite, according to reactions of the type  
 802  $24 \text{ (Mg,Fe)(Al,Cr)}_2\text{O}_4 + 18 \text{ (Mg,Fe,Al)}_3\text{Si}_2\text{O}_5(\text{OH})_4 + 12\text{H}_2\text{O} + \text{O}_2 \rightarrow$



806 (cf. Mellini et al., 2005; Merlini et al., 2009), and then overgrown by Cr-poor magnetite (Fig. 4d).  
 807 The P-T conditions for the subsequent Alpine metamorphism at Cogne are not precisely known.  
 808 However, assuming a typical subduction geothermal gradient (<10°C/km), the coexistence of  
 809 lizardite and antigorite in both serpentized peridotites and pegmatoid serpentinites suggests  
 810 temperatures not exceeding 390°C (Schwartz et al., 2013), which are too low to determine significant  
 811 mobilization of Cr.

812 Iron (Mn) oxyhydroxides and Fe sulphide deposits are the most common forms of Fe  
 813 accumulation in modern seafloor hydrothermal settings (e.g., Rona, 1988). In principle, magnetite  
 814 may form by reduction and dehydration of Fe-oxyhydroxides or by desulphurization of Fe-sulphides  
 815 during metamorphism. However, our geochronological data demonstrate that the magnetite-forming  
 816 event was coeval with the spreading of the Piedmont-Liguria ocean and thus predates Alpine  
 817 metamorphism. Also the geochemistry of Cogne magnetite ores and associated rocks contradicts the  
 818 metamorphic hypothesis. In fact, in Fe-oxyhydroxide accumulations, an enrichment in trace elements  
 819 such as P and Sr is typically observed (e.g., Hekinian et al., 1993; Puteanus et al., 1991). A similar  
 820 enrichment is indeed preserved in seafloor hydrothermal Mn-(Fe) deposits in southern Valle d’Aosta



821 ophiolites (median  $P_2O_5 = 0.06$  wt%, median Sr = 1650 ppm; Tumiati et al., 2010), which were  
822 metamorphosed up to eclogite-facies conditions ( $T = 550 \pm 60^\circ C$ ,  $P = 2.1 \pm 0.3$  GPa; Martin et al.,  
823 2008; Tumiati et al., 2015), but it is not observed in Cogne ores ( $P_2O_5 \leq 0.01$  wt%, median Sr = 1.6  
824 ppm). In the same ophiolites, sulphide (pyrite + chalcopyrite) deposits show no evidence of S  
825 mobilization and depletion linked to subduction metamorphism (Giacometti et al., 2014).  
826 Consistently, serpentinized mantle tectonites overlying the Cogne magnetite orebody are not depleted  
827 in S (Table 4).

828

### 829 *5.3. The role of the Alpine event*

830

831 The present structural position of the Cogne serpentinite, the lithological associations and the shape  
832 of the orebodies are in part the result of the tectonic activity that accompanied the Alpine orogenesis.  
833 The main magnetite orebodies at Site 1 and Site 3 behaved as rigid masses during the early ductile  
834 deformation events and they were affected by only low degrees of shear deformation, thus preserving  
835 the original textures and the proportions between magnetite and gangue minerals. The Alpine  
836 deformation was more intense at Site 2, which was probably located in a peripheral position with  
837 respect to the main orebody, where the fine-grained disseminated ores and the associated veins were  
838 dismembered into lenses. The Alpine metamorphism did not promote significant magnetite  
839 remobilization, as testified by the lack of isotopic resetting in uraninite inclusions in magnetite. The  
840 Alpine metamorphism is possibly responsible for the transformation of lizardite into antigorite, which  
841 is observed also in rocks that do not contain hydrothermal mineralization (i.e. magnetite-poor  
842 serpentinized peridotites and pegmatoid serpentinites). In any case the metamorphic temperatures  
843 were not sufficient to cause significant serpentine dehydration, since neoblastic forsterite is not  
844 widespread and is only found within the nodular ore at Site 1. The restriction of neoblastic forsterite  
845 to this specific site suggests that its formation could be related to higher temperature conditions  
846 ( $\sim 400^\circ C$ ) being attained locally during the magnetite hydrothermal event, rather than to the

847 subsequent metamorphism. Based on the above considerations, we conclude that Alpine  
848 metamorphism did not play a significant role in concentrating magnetite, although Alpine  
849 deformation may have pulled away portions of the deposit (now exposed at sites 1, 2 and 3) that could  
850 have been much closer to one another in their original oceanic setting.

851

#### 852 *5.4 Stages of formation of the Cogne deposit*

853

854 Considering all available data, we propose the following sequence of events for the formation of the  
855 Cogne deposit (Fig. 15):

856 1) Formation of an oceanic core complex made of tectonic peridotites, containing bodies of gabbros  
857 and Cr-poor melt-impregnated peridotites (troctolites).

858 2) Extensive low-temperature serpentinization, producing lizardite serpentinites containing a first  
859 generation of disseminated magnetite (Cr-bearing in mantle tectonites and Cr-free in melt  
860 impregnated peridotites). This process probably occurred at high water/rock ratios and determined  
861 the complete serpentinization of the primary silicates and an extensive loss of Ca.

862 3) Production of a high-temperature, Fe-rich hydrothermal fluid by reaction of downwelling seawater  
863 with substrate rocks. The involvement of Fe-gabbros in the reaction zone is likely, as this would  
864 enhance the content of Fe in the fluid.

865 4) Phase separation in the upwelling hydrothermal fluid, producing a more Fe-rich brine.

866 5) Reaction of the upwelling hot brine (~300–400°C) with various lithologies (serpentinites after  
867 mantle tectonites and troctolites) at various fluid/rock ratios, producing the dissolution of lizardite  
868 and the precipitation of abundant magnetite along with antigorite and clinochlore (± brucite and  
869 forsterite), forming fine-grained disseminated, nodular and massive replacive ores. Further upwelling  
870 of the magnetite-buffered fluid produced magnetite + Cu-sulphide + antigorite veins and fine-grained  
871 disseminations in shallower serpentinites.

872 6) Circulation of late fluids with higher pH and/or higher  $\text{Ca}^{2+}$  activity, producing diopside-rich,  
873 magnetite-bearing metasomatic rocks.

874

## 875 **6. Conclusions**

876

877 The Cogne magnetite deposit was formed at ~150 Ma by hydrothermal processes during an advanced  
878 stage of the opening of the Piedmont–Liguria ocean. Based on geological and petrographic features  
879 and on geochemical and mineralogical similarities with some modern ultramafic-hosted VMS  
880 deposits on mid-ocean ridges, the exposed mineralized section at Cogne may represent the deep  
881 segment of a seafloor, high-temperature (~300–400°C) hydrothermal system, which was possibly  
882 associated with shallower, now eroded, sulphide-rich bodies (Fig. 15). As suggested by  
883 thermodynamic modelling, simple seawater-rock interactions cannot produce the Fe endowment  
884 observed at Cogne. Fractionation processes such as phase separation were probably critical to  
885 generate sufficiently Fe-rich hydrothermal fluids capable to precipitate large amounts of magnetite in  
886 various types of mantle host-rocks. The possible occurrence of similar ultramafic-hosted magnetite  
887 deposits in present-day oceanic settings could contribute to explain the presence of significant  
888 magnetic anomalies centred on active and inactive ultramafic-hosted hydrothermal fields (Fujii et al.,  
889 2016; Szitkar et al., 2014; Tivey and Dymant, 2010).

890

891

## 892 **Acknowledgements**

893

894 We thank Raul Carampin (CNR, IGG, Padua) and Andrea Risplendente (Earth Sciences Department,  
895 University of Milan) for the technical assistance with the electron microprobe analyses. We are also  
896 grateful to Drs. Andreas Klügel and Patrick Monien (“Petrology of the Ocean Crust” research group,

897 University of Bremen, Germany) for providing scientific and technical support during LA-ICP-MS  
898 measurements. We thank “Assessorato Territorio e Ambiente” of the Valle d’Aosta region for  
899 providing access to the archives of the Cogne mine. We are grateful to Patrick Nadoll and Paola  
900 Tartarotti for their constructive reviews and suggestions. This work was carried out during LT’s PhD  
901 at the University of Padua. PN acknowledges financial support by Progetto di Ateneo 2013  
902 CPDA138741 “Copper metallogenesis and provenancing in the Alpine realm” (University of Padua).

903

904

## 905 **References**

906

907 Alexandre P and Kyser TK (2005) Effects of cationic substitutions and alteration in uraninite, and  
908 implications for the dating of uranium deposits. *Can Mineral* 43:1005–1017

909

910 Andreani M, Escartin J, Delacour A, Ildefonse B, Godard M, Dymant J, Fallick AE, Fouquet Y (2014)  
911 Tectonic structure, lithology, and hydrothermal signature of the Rainbow massif (Mid-Atlantic Ridge  
912 36° 14’ N). *Geochem Geophys Geosy* 15:3543–3571

913

914 Arai S, Akizawa N (2014) Precipitation and dissolution of chromite by hydrothermal solutions in the  
915 Oman ophiolite: New behavior of Cr and chromite. *Am Mineral* 99:28–34

916

917 Bach W, Klein F (2009) The petrology of seafloor rodingites: insights from geochemical reaction  
918 path modeling. *Lithos*, 112:103–117

919

920 Bédard JH, Hébert R (1998) Formation of chromitites by assimilation of crustal pyroxenites and  
921 gabbros into peridotitic intrusions: North Arm Mountain massif, Bay of Islands ophiolite,  
922 Newfoundland, Canada. *J Geophys Res-Sol Ea* 103:5165–5184

923

924 Benciolini L, Lombardo B, Martin S (1988) Mineral chemistry and Fe/Mg exchange geothermometry  
925 of ferrogabbro-derived eclogites from the Northwestern Alps. *Neues Jb Miner Abh* 159:199–222

926

927 Berkenbosch HA, de Ronde CEJ, Gemmel JB, McNeil AW, Goemann K (2012) Mineralogy and  
928 formation of black smoker chimneys from Brothers submarine volcano, Kermadec Arc. *Econ Geol*  
929 107:1613–1633

930

931 Berndt ME, Seyfried WE, Janecky DR (1989) Plagioclase and epidote buffering of cation ratios in  
932 mid-ocean ridge hydrothermal fluids: experimental results in and near the supercritical region.  
933 *Geochim Cosmochim Acta* 53:2283–2300

934

935 Bischoff JL, Rosenbauer RJ (1987) Phase separation in seafloor geothermal systems; an experimental  
936 study of the effects on metal transport. *Am J Sci* 287:953–978

937

938 Blackman DK, Ildefonse B, John BE, Ohara Y, Miller DJ, MacLeod CJ and Expedition 304/305  
939 Scientists (2006) Proceedings of the Integrated Ocean Drilling Program, Volume 304/305, College  
940 Station, Texas, Integrated Ocean Drilling Program Management International, Inc.

941

942 Bocchio R, Benciolini L, Martin S, Tartarotti P (2000) Geochemistry of eclogitised Fe-Ti gabbros  
943 from various lithological settings (Aosta Valley ophiolites, Italian western Alps). *Protolith*  
944 composition and eclogitic paragenesis. *Period Mineral* 69:217–237

945

946 Bodinier J-L and Godard M (2003) Orogenic, ophiolitic, and abyssal peridotites. In: Turekian KK  
947 and Holland HD (eds) *The Mantle and Core: Treatise on Geochemistry*, 2nd edn. Elsevier, Oxford,  
948 pp 103-167

949

950 Boschi C, Früh-Green GL, Delacour A, Karson JA, Kelley DS (2006) Mass transfer and fluid flow  
951 during detachment faulting and development of an oceanic core complex, Atlantis Massif (MAR  
952 30°N). *Geochem Geophys Geosys* 7

953

954 Boutroy E, Dare SA, Beaudoin G, Barnes SJ, Lightfoot PC (2014) Magnetite composition in Ni-Cu-  
955 PGE deposits worldwide: application to mineral exploration. *J Geochem Explor* 145:64–81

956

957 Bowles JFW (1990). Age dating of individual grains of uraninite in rocks from electron microprobe  
958 analyses. *Chem Geol* 83:47–53

959

960 Bowles JF (2015) Age Dating from Electron Microprobe Analyses of U, Th, and Pb: Geological  
961 Advantages and Analytical Difficulties. *Microsc Microanal* 21:1114–1122

962

963 Caby R (1981) Le Mésozoïque de la zone du Combin en Val d'Aoste (Alpes Graies): imbrications  
964 tectoniques entre séries issues des domaines pennique, austroalpin et océanique. *Géologie Alpine*  
965 57:5–13

966

967 Carbonin S, Martin S, Tumiati S, Rossetti P (2014) Magnetite from the Cogne serpentinites (Piemonte  
968 ophiolite nappe, Italy). Insights into seafloor fluid–rock interaction. *Eur J Mineral* 27:31–50

969

970 Caruso LJ, Chernosky JV (1979) The stability of lizardite. *Can Mineral* 17:757–769

971

972 Castello P, Dal Piaz GV, Gosso G, Kienast JR, Martin S, Natale P, Nervo R, Polino R, Venturelli G  
973 (1980) The Piedmont ophiolite nappe in the Aosta Valley and related ore deposits. In: Gruppo di

974 Lavoro sulle Ofioliti Mediterranee. VI ophiolite field conference, Firenze. Field excursion book, pp.  
975 171–192  
976  
977 Castello P (1981) Inventario delle mineralizzazioni a magnetite, ferro-rame e manganese del  
978 complesso piemontese dei calcescisti con pietre verdi in Valle d’Aosta. *Ofioliti* 6:5–46  
979  
980 Charlou JL, Donval JP, Fouquet Y, Jean-Baptiste P, Holm N (2002) Geochemistry of high H<sub>2</sub> and  
981 CH<sub>4</sub> vent fluids issuing from ultramafic rocks at the Rainbow hydrothermal field (36°14’N, MAR).  
982 *Chem Geol* 191:345–359  
983  
984 Cocherie A and Albarede F (2001) An improved U-Th-Pb age calculation for electron microprobe  
985 dating of monazite. *Geochim Cosmochim Acta* 65:4509–4522  
986  
987 Cocherie A and Legendre O (2007) Potential minerals for determining U–Th–Pb chemical age using  
988 electron microprobe. *Lithos* 93:288–309  
989  
990 Compagnoni R, Elter G, Fiora L, Natale P, Zucchetti S (1979) Nuove osservazioni sul giacimento di  
991 magnetite di Cogne in Valle d’Aosta. *Rend Soc Min Petr* 35:755–766  
992  
993 Compagnoni R, Elter G, Fiora L, Natale P, Zucchetti S (1981) Magnetite deposits in serpentinized  
994 lherzolites from the ophiolitic belt of the Western Alps, with special reference to the Cogne deposit  
995 (Aosta Valley). In: *Proceedings of the Intern. Symp. Mafic and Ultramafic Complexes, Athens*, pp  
996 376–394  
997

998 Cordey F, Tricart P, Guillot S, Schwartz S (2012) Dating the Tethyan Ocean in the Western Alps  
999 with radiolarite pebbles from synorogenic Oligocene molasse basins (southeast France). *Swiss J*  
1000 *Geosci* 105:39–48  
1001

1002 Cortiana G, Dal Piaz GV, Del Moro A, Hunziker JC, Martin S (1998)  $^{40}\text{Ar}$ - $^{39}\text{Ar}$  and Rb-Sr dating  
1003 of the Pillonet klippe and Sesia-Lanzo basal slice in the Ayas valley and evolution of the  
1004 Austroalpine-Piedmont nappe stack. *Memorie di Scienze Geologiche* 50:177–194  
1005

1006 Cross A, Jaireth S, Rapp R, Armstrong R (2011). Reconnaissance-style EPMA chemical U–Th–Pb  
1007 dating of uraninite. *Austr J Earth Sci* 58:675–683  
1008

1009 Dal Piaz G, Cortiana G, Del Moro A, Martin S, Pennacchioni G, Tartarotti P (2001) Tertiary age and  
1010 paleostructural inferences of the eclogitic imprint in the Austroalpine outliers and Zermatt–Saas  
1011 ophiolite, western Alps. *Int J Earth Sci* 90:668–684  
1012

1013 Dal Piaz GV, Bistacchi A, Massironi M (2003) Geological outline of the Alps. *Episodes* 26:175–180  
1014

1015 Dal Piaz GV, Gianotti F, Monopoli B, Pennacchioni G, Tartarotti P, Schiavo A (2010) Note  
1016 illustrative della carta geologica d'Italia alla scala 1:50.000 Chatillon F. 91. Ispra-Servizio Geologico  
1017 d'Italia, Treviso  
1018

1019 Dare SA, Barnes SJ, Beaudoin G, Méric J, Boutroy E, Potvin-Doucet C (2014) Trace elements in  
1020 magnetite as petrogenetic indicators. *Miner Deposita* 49:785–796  
1021



1022 Debret B, Andreani M, Muñoz M, Bolfan-Casanova N, Carlut J, Nicollet C, Schwartz S, Trcera N  
1023 (2014) Evolution of Fe redox state in serpentine during subduction. *Earth Planet Sci Lett* 400:206–  
1024 218  
1025

1026 De Giusti F, Dal Piaz GV, Massironi M, Schiavo A (2003) Carta geotettonica della Valle d'Aosta.  
1027 *Mem Sci Geol* 55:129–49  
1028

1029 De Graciansky PC, Roberts D, Tricart P (2011) The Western Alps from rift to passive margin to  
1030 orogenic belt: An integrated geosciences overview. Elsevier, Amsterdam  
1031

1032 Della Giusta A, Carbonin S, Russo U (2011) Chromite to magnetite transformation: compositional  
1033 variations and cation distributions (southern Aosta Valley, Western Alps, Italy). *Period Mineral* 80:1–  
1034 17  
1035

1036 de Ronde CEJ, Massoth GJ, Butterfield DA, Christenson BW, Ishibashi J, Ditchburn RG, Hannington  
1037 MD, Brathwaite RL, Lupton JE, Kamenetsky VS, Graham IJ, Zellmer GF, Dziak RP, Embley RW,  
1038 Dekov VM, Munnik F, Lahr J, Evans LJ, Takai K (2011) Submarine hydrothermal activity and gold-  
1039 rich mineralization at Brothers Volcano, Kermadec Arc, New Zealand. *Miner Deposita* 46:541–584  
1040

1041 Di Colbertaldo D, Di Furia E, Rossi F (1967) Il giacimento a magnetite di Cogne in Val d'Aosta.  
1042 Istituto Lombardo, A101:361–394  
1043

1044 Diella V, Ferrario A, Rossetti P (1994) The magnetite ore deposits of the southern Aosta Valley:  
1045 chromitite transformed during an Alpine metamorphic event. *Ofioliti* 19:247–256  
1046

1047 Ding K, Seyfried WE (1992) Determination of Fe-Cl complexing in the low pressure supercritical  
1048 region (NaCl fluid): Iron solubility constraints on pH of seafloor hydrothermal fluids. *Geochim*  
1049 *Cosmochim Acta* 56:3681–3692  
1050

1051 Douville E, Charlou JL, Oelkers EH, Bienvenu P, Colon CJ, Donval JP, Fouquet Y, Prieur D, Appriou  
1052 P (2002) The rainbow vent fluids (36° 14' N, MAR): the influence of ultramafic rocks and phase  
1053 separation on trace metal content in Mid-Atlantic Ridge hydrothermal fluids. *Chem Geol* 184:37–48  
1054  
1055

1056 Drouin M, Godard M, Ildefonse B, Bruguier O, Garrido CJ (2009) Geochemical and petrographic  
1057 evidence for magmatic impregnation in the oceanic lithosphere at Atlantis Massif, Mid-Atlantic  
1058 Ridge (IODP Hole U1309D, 30° N). *Chem Geol* 264:71–88.  
1059

1060 Dupuis C, Beaudoin G (2011) Discriminant diagrams for iron oxide trace element fingerprinting of  
1061 mineral deposit types. *Miner Deposita* 46:319–335  
1062

1063 Edmonds H (2010) Chemical signatures from hydrothermal venting on slow spreading ridges. In:  
1064 Rona PA, Devey CW, Dymant J, Murton BJ (eds) *Diversity of hydrothermal systems on slow*  
1065 *spreading ocean ridges*, American Geophysical Union, Washington, DC, pp. 27–42  
1066

1067 Evans BW (2004) The serpentinite multisystem revisited: chrysotile is metastable. *Int Geol Rev*  
1068 46:479–506  
1069

1070 Evans BW (2010) Lizardite versus antigorite serpentinite: magnetite, hydrogen, and life (?). *Geology*  
1071 38:879–882  
1072

1073 Fantone I, Grieco G, Strini A, Cavallo A (2014) The effect of Alpine metamorphism on an oceanic  
1074 Cu-Fe sulfide ore: the Herin deposit, Western Alps, Italy. *Period Mineral* 83:345–365  
1075

1076 Filzmoser P, Hron K, Reimann C (2009) Principal component analysis for compositional data with  
1077 outliers. *Environmetrics* 20:621–632  
1078

1079 Filzmoser P, Hron K (2011) Robust statistical analysis. In: Pawlowsky-Glahn V, Buccianti A (eds)  
1080 Compositional data analysis. Theory and applications. John Wiley & Sons, Chichester (UK), pp. 59-  
1081 72  
1082

1083 Fontana E, Panseri M, Tartarotti P (2008) Oceanic relict textures in the Mount Avic serpentinites,  
1084 Western Alps. *Ofioliti* 33:105–118  
1085

1086 Fontana E, Tartarotti P, Panseri M, Buscemi S (2015) Geological map of the Mount Avic massif  
1087 (Western Alps Ophiolites). *Journal of Maps* 11:126–135  
1088

1089 Fouquet Y, Cambon P, Etoubleau J, Charlou JL, Ondréas H, Barriga FJAS, Cherkashov G, Semkova  
1090 T, Poroshina I, Bohn M, Donval JP, Henry K, Murphy P, Rouxel O (2010) Geodiversity of  
1091 hydrothermal processes along the Mid-Atlantic Ridge and ultramafic-hosted mineralization: a new  
1092 type of oceanic Cu-Zn-Co-Au volcanogenic massive sulfide deposit. In: Rona PA, Devey CW,  
1093 Dymont J, Murton BJ (eds) Diversity of hydrothermal systems on slow spreading ocean ridges,  
1094 American Geophysical Union, Washington, DC, pp. 321–367  
1095

1096 Foustoukos DI, Seyfried WE (2007) Fluid phase separation processes in submarine hydrothermal  
1097 systems. *Rev Mineral Geochem* 65:213–239  
1098

1099 Frost BR, Beard JS (2007) On silica activity and serpentinization. *J Petrol* 48:1351–1368  
1100

1101 Fujii M, Okino K, Sato T, Sato H, Nakamura K (2016) Origin of magnetic highs at ultramafic hosted  
1102 hydrothermal systems: Insights from the Yokoniwa site of Central Indian Ridge. *Earth Planet Sci Lett*  
1103 441:26–37  
1104

1105 Gahlan HA, Arai S, Ahmed AH, Ishida Y, Abdel-Aziz YM, Rahimi A (2006) Origin of magnetite  
1106 veins in serpentinite from the Late Proterozoic Bou-Azzer ophiolite, Anti-Atlas, Morocco: An  
1107 implication for mobility of iron during serpentinization. *J Afr Earth Sci* 46: 318–330  
1108

1109 Giacometti F, Evans KA, Rebay G, Cliff J, Tomkins AG, Rossetti P, Vaggelli G, Adams DT (2014)  
1110 Sulfur isotope evolution in sulfide ores from Western Alps: Assessing the influence of subduction-  
1111 related metamorphism. *Geochem Geophys Geosys* 15:3808–3829  
1112

1113 Govindaraju K (1994) compilation of working values and sample description for 383 geostandards.  
1114 *Geostandard Newslett* 18:1–158  
1115

1116 Groppo C, Rinaudo C, Cairo S, Gastaldi D, Compagnoni R (2006) Micro-Raman spectroscopy for a  
1117 quick and reliable identification of serpentine minerals from ultramafics. *Eur J of Mineral* 18:319–  
1118 329  
1119

1120 Hekinian R, Hoffert M, Larque P, Cheminee JL, Stoffers P, Bideau D (1993) Hydrothermal Fe and  
1121 Si oxyhydroxide deposits from South Pacific intraplate volcanoes and East Pacific Rise axial and off-  
1122 axial regions. *Econ Geol* 88:2099–2121  
1123

1124 Hiess J, Condon DJ, McLean N, Noble SR (2012)  $^{238}\text{U}/^{235}\text{U}$  systematics in terrestrial uranium-  
1125 bearing minerals. *Science* 335:1610–1614  
1126

1127 Ho PC, Palmer DA, Mesmer RE (1994) Electrical conductivity measurements of aqueous sodium  
1128 chloride solutions to 600 C and 300 MPa. *J Solution Chem* 23:997–1018  
1129

1130 Ho PC, Bianchi H, Palmer DA, Wood RH (2000) Conductivity of dilute aqueous electrolyte solutions  
1131 at high temperatures and pressures using a flow cell. *J Solution Chem* 29: 217–235  
1132

1133 Ho PC, Palmer DA, Gruszkiewicz MS (2001) Conductivity measurements of dilute aqueous HCl  
1134 solutions to high temperatures and pressures using a flow-through cell. *J Phys Chem B* 105:1260–  
1135 1266  
1136

1137 Ildefonse B, Blackman DK, John BE, Ohara Y, Miller DJ, MacLeod CJ (2007) Oceanic core  
1138 complexes and crustal accretion at slow-spreading ridges. *Geology* 35: 623–626  
1139

1140 Jaffey AH, Flynn KF, Glendenin LE, Bentley WT., Essling AM (1971) Precision measurement of  
1141 half-lives and specific activities of  $^{235}\text{U}$  and  $^{238}\text{U}$ . *Phys Rev C* 4:1889  
1142

1143 Jupp TE, Schultz A (2004) Physical balances in subseafloor hydrothermal convection cells. *J*  
1144 *Geophys Res-Sol Earth* 109(B5)  
1145

1146 Klein F, Bach W, Jöns N, McCollom T, Moskowitz B, Berquó T (2009) Iron partitioning and  
1147 hydrogen generation during serpentinization of abyssal peridotites from 15 N on the Mid-Atlantic  
1148 Ridge. *Geochim Cosmochim Ac* 73:6868–6893  
1149

1150 Le Maitre RW (1982) Numerical Petrology, Statistical Interpretation of Geochemical Data. Elsevier,  
1151 Amsterdam  
1152  
1153 Le Roux LJ, Glendenin LE (1963). Half-life of  $^{232}\text{Th}$ . In: Proceedings of the National Meeting on  
1154 Nuclear Energy: Application of Isotopes and Radiation, Pretoria, pp 83–94  
1155 Lombardo B, Pognante U (1982) Tectonic implications in the evolution of the Western Alps ophiolite  
1156 metagabbros. *Ofioliti* 2:371–394  
1157  
1158 Lombardo B, Rubatto D, Castelli D (2002) Ion microprobe U-Pb dating of zircon from a Monviso  
1159 metaplagiognanite: implications for the evolution of the Piedmont-Liguria Tethys in the Western  
1160 Alps. *Ofioliti* 27:109–117  
1161  
1162 Ludwig K. R. (2012) User's manual for ISOPLOT 3.75, a geochronological toolkit for Microsoft  
1163 Excel. Berkeley Geochronology Center, Spec. Pub. 5  
1164  
1165 Manatschal G, Müntener O (2009) A type sequence across an ancient magma-poor ocean–continent  
1166 transition: the example of the western Alpine Tethys ophiolites. *Tectonophysics* 473:4–19  
1167  
1168 Manatschal G, Sauter D, Karpoff AM, Masini E, Mohn G, Lagabriele Y (2011) The Chenaillet  
1169 Ophiolite in the French/Italian Alps: an ancient analogue for an oceanic core complex? *Lithos*  
1170 124:169–184  
1171  
1172 Marques AFA (2005) Geology and genesis of sulfide mineralization in the Rainbow ultramafic-  
1173 hosted seafloor hydrothermal system. Dissertation, University of Lisbon  
1174

1175 Marques AFA, Barriga FJ, Chavagnac V, Fouquet Y (2006) Mineralogy, geochemistry, and Nd  
1176 isotope composition of the Rainbow hydrothermal field, Mid-Atlantic Ridge. *Miner Deposita* 41:52–  
1177 67  
1178

1179 Marques AFA, Barriga FJ, Scott SD (2007) Sulfide mineralization in an ultramafic-rock hosted  
1180 seafloor hydrothermal system: From serpentinization to the formation of Cu–Zn–(Co)-rich massive  
1181 sulfides. *Mar Geol* 245:20–39  
1182

1183 Martin S, Rebay G, Kienast J, Mével C (2008) An eclogitised oceanic palaeo-hydrothermal field from  
1184 the St. Marcel Valley (Italian Western Alps). *Ofioliti* 33:49–63  
1185

1186 McCaig AM, Cliff RA, Escartin J, Fallick AE, MacLeod CJ (2007) Oceanic detachment faults focus  
1187 very large volumes of black smoker fluids. *Geology* 35:935–938  
1188

1189 McDonough WF, Sun S (1995) The composition of the Earth. *Chem Geol* 120:223–253  
1190

1191 Melekestseva IY, Zaykov VV, Nimis P, Tret'yakov GA, Tessalina SG (2013) Cu–(Ni–Co–Au)-  
1192 bearing massive sulfide deposits associated with mafic–ultramafic rocks of the Main Urals Fault,  
1193 South Urals: Geological structures, ore textural and mineralogical features, comparison with modern  
1194 analogs. *Ore Geol Rev* 52:18–36  
1195

1196 Melekestseva IY, Tret'yakov GA, Nimis P, Yuminov AM, Maslennikov VV, Maslennikova SP,  
1197 Kotlyarov VA, Beltenev VE, Danyushevsky LV, Large R (2014) Barite-rich massive sulfides from  
1198 the Semenov-1 hydrothermal field (Mid-Atlantic Ridge, 13°30.87'N): Evidence for phase separation  
1199 and magmatic input. *Mar Geol* 349:37–54  
1200

1201 Mellini M, Rumori C, Viti C (2005) Hydrothermally reset magmatic spinels in retrograde  
1202 serpentinites: formation of “ferritchromit” rims and chlorite aureoles. *Contrib Mineral Petr* 149:266–  
1203 275  
1204

1205 Merlini A, Grieco G, Diella V (2009) Ferritchromite and chromian-chlorite formation in mélange-  
1206 hosted Kalkan chromitite (Southern Urals, Russia). *Am Mineral* 94:1459–1467  
1207

1208 Mével C (2003) Serpentinization of abyssal peridotites at mid-ocean ridges. *C R Geosci* 335:825–  
1209 852  
1210

1211 Montel JM, Foret S, Veschambre M, Nicollet C, Provost A (1996) Electron microprobe dating of  
1212 monazite. *Chem Geol* 131:37–53  
1213

1214 Nadoll P, Koenig AE (2011) LA-ICP-MS of magnetite: methods and reference materials. *J Anal*  
1215 *Atom Spectrom* 26:1872–1877  
1216

1217 Nadoll P, Angerer T, Mauk JL, French D, Walshe J (2014) The chemistry of hydrothermal magnetite:  
1218 a review. *Ore Geol Rev* 61:1–32  
1219

1220 Nadoll P, Mauk JL, Leveille RA, Koenig AE (2015) Geochemistry of magnetite from porphyry Cu  
1221 and skarn deposits in the southwestern United States. *Miner Deposita* 50:493–515  
1222

1223 Niu Y (2004) Bulk-rock major and trace element compositions of abyssal peridotites: implications  
1224 for mantle melting, melt extraction and post-melting processes beneath mid-ocean ridges. *J Petrol*  
1225 45:2423–2458  
1226



1227 O'Neill HSC, Palme H (1998) Composition of the silicate Earth: implications for accretion and core  
1228 formation. In: Jackson I (ed) *The Earth's mantle: composition, structure and evolution*, Cambridge  
1229 University Press, pp. 3–126  
1230

1231 Panseri M, Fontana E, Tartarotti P (2008) Evolution of rodingitic dykes: metasomatism and  
1232 metamorphism in the Mount Avic serpentinites (Alpine Ophiolites, southern Aosta Valley). *Ofioliti*,  
1233 33:165–185  
1234

1235 Paraskevopoulos GM, Economou M (1980) Genesis of magnetite ore occurrences by metasomatism  
1236 of chromite ores in Greece. *Neues Jb Miner Abh* 140:29–53  
1237

1238 Paulick H, Bach W, Godard M., De Hoog JCM, Suhr G, Harvey J (2006) Geochemistry of abyssal  
1239 peridotites (Mid-Atlantic Ridge, 15 20' N, ODP Leg 209): implications for fluid/rock interaction in  
1240 slow spreading environments. *Chem Geol* 234:179–210  
1241

1242 Pester NJ, Ding K, Seyfried WE (2014) Magmatic eruptions and iron volatility in deep-sea  
1243 hydrothermal fluids. *Geology* 42:255–258  
1244

1245 Piccardo, G-B. (2008) The Jurassic Ligurian Tethys, a fossil ultraslow-spreading ocean: the mantle  
1246 perspective. In: Coltorti M, Grégoire M (Eds) *Metamorphism in oceanic and continental lithospheric*  
1247 *mantle*. Geological Society, London, Special Publication, vol. 293, pp. 11–33  
1248

1249 Polino R, Martin S, Malusà M, Mosca P, Bonetto F, Baggio P, Baster I, Bertolo D, Carraro F, Fontan  
1250 D, Gianotti F, Monopoli B, Perello P, Schiavo A, Venturini G, Vuillermoz R (2014) Note illustrative  
1251 della carta geologica d'Italia alla scala 1:50.000 Aosta F. 90. Ispra-Servizio Geologico d'Italia  
1252

1253 Puteanus D, Glasby GP, Stoffers P, Kunzendorf H (1991) Hydrothermal iron-rich deposits from the  
1254 Teahitia-Mehitia and Macdonald hot spot areas, Southwest Pacific. *Mar Geol* 98:389–409  
1255

1256 Renna MR, Tribuzio R (2011) Olivine-rich troctolites from Ligurian ophiolites (Italy): evidence for  
1257 impregnation of replacive mantle conduits by MORB-type melts. *J Petrol* 52:1763–1790  
1258

1259 Rollinson H (1993) *Using geochemical data*. Longman, London  
1260

1261 Rona PA (1988) Hydrothermal mineralization at oceanic ridges. *Can Mineral* 26:431–465  
1262

1263 Rossetti P, Gatta GD, Diella V, Carbonin S, Della Giusta A, Ferrario A (2009) The magnetite ore  
1264 districts of the southern Aosta Valley (Western Alps, Italy): a mineralogical study of metasomatized  
1265 chromite ore. *Mineral Mag* 73:737–751  
1266

1267 Routhier P (1963) *Les gisements métallifères: géologie et principes de recherche*. Masson, Paris  
1268

1269 Sanfilippo A, Tribuzio R (2013) Building of the deepest crust at a fossil slow-spreading centre (Pineto  
1270 gabbroic sequence, Alpine Jurassic ophiolites). *Contrib Mineral Petr* 165:705–721  
1271

1272 Sanfilippo A, Tribuzio R, Tiepolo M (2014) Mantle–crust interactions in the oceanic lithosphere:  
1273 Constraints from minor and trace elements in olivine. *Geochim Cosmochim Acta* 141:423–439  
1274

1275 Sawyer GM, Oppenheimer C, Tsanev VI, Yirgu G (2008) Magmatic degassing at Erta'Ale volcano,  
1276 Ethiopia. *J Volcanol Geoth Res* 178:837–846  
1277

1278 Schmid SM, Fügenschuh B, Kissling E, Schuster R (2004) Tectonic map and overall architecture of  
1279 the Alpine orogen. *Eclogae Geol Helv* 97:93–117  
1280

1281 Schwartz S, Guillot S, Reynard B, Lafay R, Debret B, Nicollet C, Lanari P, Auzende AL (2013)  
1282 Pressure–temperature estimates of the lizardite/antigorite transition in high pressure serpentinites.  
1283 *Lithos* 178:197–210  
1284

1285 Seyfried Jr WE (1987) Experimental and theoretical constraints on hydrothermal alteration processes  
1286 at mid-ocean ridges. *Annu Rev Earth Pl Sc* 15:317  
1287

1288 Seyfried WE, Foustoukos DI, Allen DE (2004) Ultramafic-hosted hydrothermal systems at mid-ocean  
1289 ridges: chemical and physical controls on pH, redox and carbon reduction reactions. In: German CR,  
1290 Lin J, Parson LM (eds) *Mid-ocean ridges: hydrothermal interactions between the lithosphere and*  
1291 *oceans*, American Geophysical Union, Washington, DC, pp. 267–284  
1292

1293 Seyfried WE, Pester N, Fu Q (2010) Phase equilibria controls on the chemistry of vent fluids from  
1294 hydrothermal systems on slow spreading ridges: reactivity of plagioclase and olivine solid solutions  
1295 and the pH-silica connection. In: Rona PA, Devey CW, Dymant J, Murton BJ (eds) *Diversity of*  
1296 *hydrothermal systems on slow spreading ocean ridges*, American Geophysical Union, Washington,  
1297 DC, pp. 297-320  
1298

1299 Seyfried WE, Pester NJ, Ding K, Rough M (2011) Vent fluid chemistry of the Rainbow hydrothermal  
1300 system (36 N, MAR): phase equilibria and in situ pH controls on seafloor alteration processes.  
1301 *Geochim Cosmochim Ac* 75:1574–1593  
1302

1303 Singh SC, Crawford WC, Carton H, Seher T, Combier V, Cannat M, Canales JP, Düşünür D, Escartin  
1304 J, Miranda JM (2006). Discovery of a magma chamber and faults beneath a Mid-Atlantic Ridge  
1305 hydrothermal field. *Nature* 442:1029–1032  
1306

1307 Suhr G, Hellebrand E, Johnson K, Brunelli D (2008) Stacked gabbro units and intervening mantle: A  
1308 detailed look at a section of IODP Leg 305, Hole U1309D. *Geochem Geophys Geosy* 9  
1309

1310 Szitkar F, Dymant J, Fouquet Y, Honsho C, Horen H (2014) The magnetic signature of ultramafic-  
1311 hosted hydrothermal sites. *Geology* 42:715–718  
1312

1313 Stampfli GM (2000) Tethyan oceans. *Geol Soc Spec Publ* 173:1–23  
1314

1315 Stella A (1916) *Le miniere di Cogne (Val d'Aosta)*. S.A.I.G. A. Barabino, Genova  
1316

1317 Tartarotti P, Festa A, Benciolini L, Balestro G (2015) Mantle-cover sequence in the Western Alps  
1318 metaophiolites: a key to recognize remnants of an exhumed Oceanic Core Complex (OCC). *Rend*  
1319 *Online Soc Geol It, Suppl. n. 2, Vol. 35*  
1320

1321 Tivey MA, Dymant J (2010) The magnetic signature of hydrothermal systems in slow spreading  
1322 environments. In: *Diversity of Hydrothermal Systems on Slow Spreading Ocean Ridges*. In: Rona  
1323 PA, Devey CW, Dymant J, Murton BJ (eds) *Diversity of hydrothermal systems on slow spreading*  
1324 *ocean ridges*, American Geophysical Union, Washington, DC, pp. 43–66  
1325

1326 Tumiatì S, Martin S, Godard G (2010) Hydrothermal origin of manganese in the high-pressure  
1327 ophiolite metasediments of Praborna ore deposit (Aosta Valley, Western Alps). *Eur J Mineral*  
1328 22:577–594

1329

1330 Tumiati S, Godard G, Martin S, Malaspina N, Poli S (2015) Ultra-oxidized rocks in subduction  
1331 mélanges? Decoupling between oxygen fugacity and oxygen availability in a Mn-rich metasomatic  
1332 environment. *Lithos* 226:116–130

1333

1334 Von Damm KL (2004) Evolution of the hydrothermal system at East Pacific Rise 9°50'N:  
1335 geochemical evidence for changes in the upper oceanic crust. In: German CR, Lin J, Parson LM (eds)  
1336 Mid-ocean ridges: hydrothermal interactions between the lithosphere and oceans, American  
1337 Geophysical Union, Washington, DC, pp. 285–304

1338

1339 Werner CD (1997). Data report: geochemistry of rocks and minerals of the gabbro complex from the  
1340 Kane area (MARK). In: Karson JA, Cannat M, Miller DJ, Elthon D (eds) Proceedings of the Ocean  
1341 Drilling Program. Scientific Results (Vol. 153). Ocean Drilling Program, pp. 457–470

1342

1343 Whitney DL, Evans BW (2010) Abbreviations for names of rock-forming minerals. *Am Mineral*  
1344 95:185–187

1345

1346 Wolery TJ, Jarek RL (2003) Software User's Manual EQ3/6 (Version 8.0). Sandia National  
1347 Laboratories, Albuquerque, New Mexico

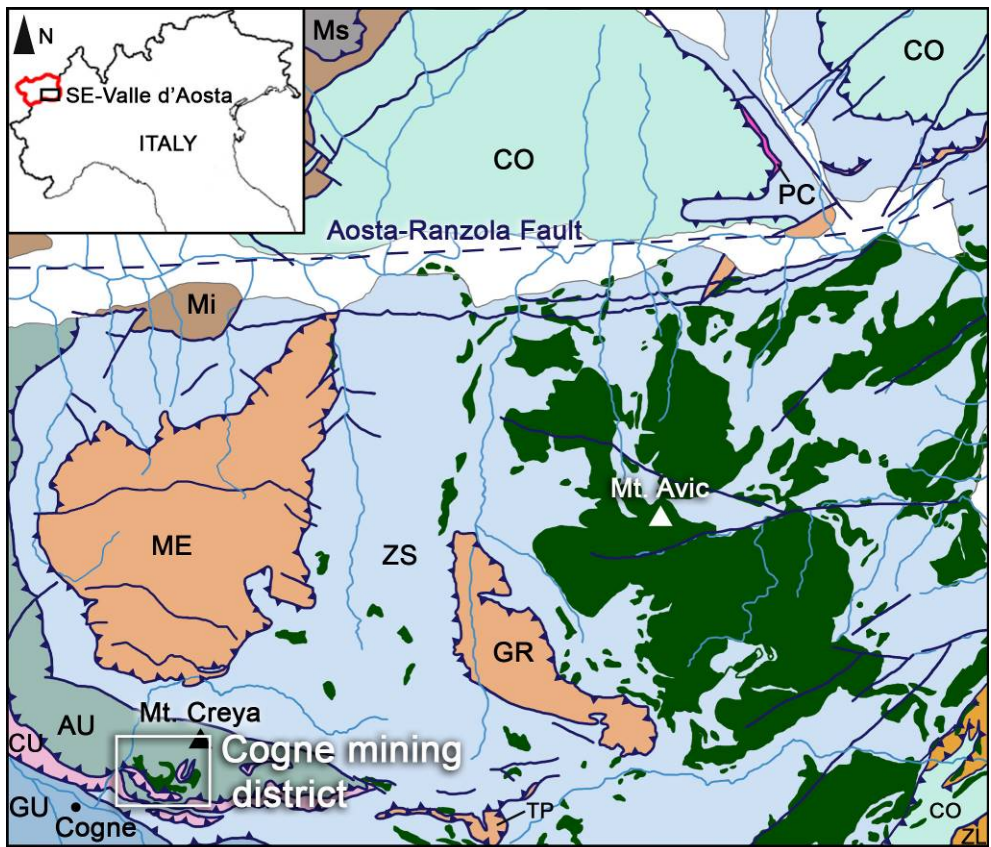
1348

1349 Wolery TJ (2013) EQ3/6 - Software for Geochemical Modeling, Version 8.0a. Lawrence Livermore  
1350 National Laboratory, Livermore, California

1351

1352 Yıldırım N, Dönmez C, Kang J, Lee I, Pirajno F, Yıldırım E, Günay K, Seo JH, Farquhar J, Chang,  
1353 SW (2016) A magnetite-rich Cyprus-type VMS deposit in Ortaklar: A unique VMS style in the  
1354 Tethyan metallogenic belt, Gaziantep, Turkey. *Ore Geol Rev* 79:425–442





CONTINENTAL CRUST  
UNITS (i.e. Austroalpine)

ECLOGITIC

ME: Mont Emilius Unit  
GR: Glacier-Rafray Unit  
TP: Tour Ponton Unit

NON-ECLOGITIC

Ms: Upper Mont Mary Unit  
Mi: Lower Mont Mary Unit

SESIA LANZO ZONE (ZL)

OPHIOLITIC UNITS

ECLOGITIC

ZS: Zermatt-Saas Unit  
GU: Grivola-Urtier Unit

NON-ECLOGITIC

AU: Aouilietta Unit  
CO: Combin Unit

■ Serpentinites

CONTINENTAL MARGIN  
UNITS

CU: Cogne Unit  
PC: Pancherot-Cime Bianche  
Unit

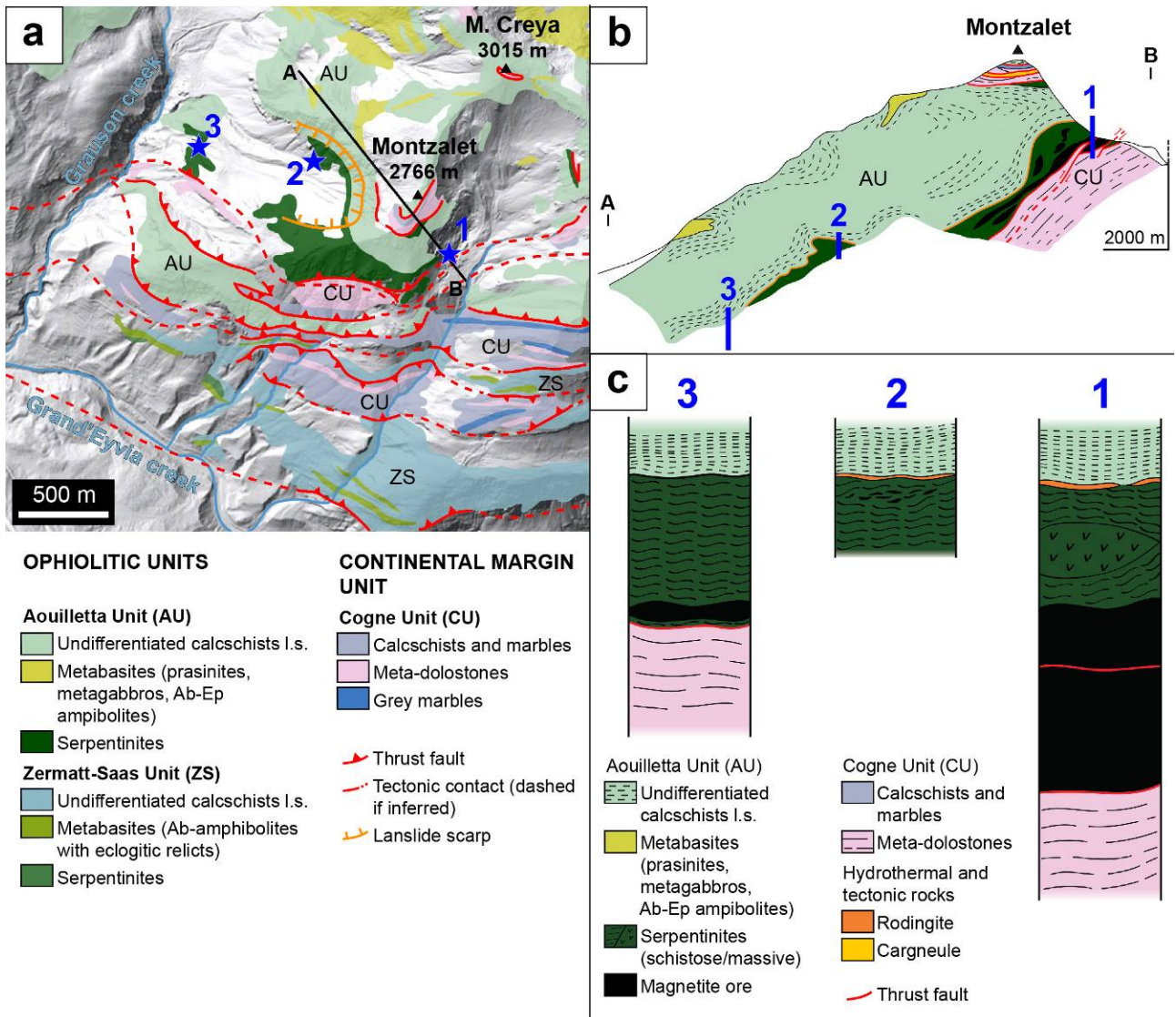
— Fault

▲ Thrust fault

1356

1357 **Fig. 1** Geological map of the southern Valle d'Aosta region. Redrawn and modified after Dal Piaz et  
1358 al. (2010).

1359

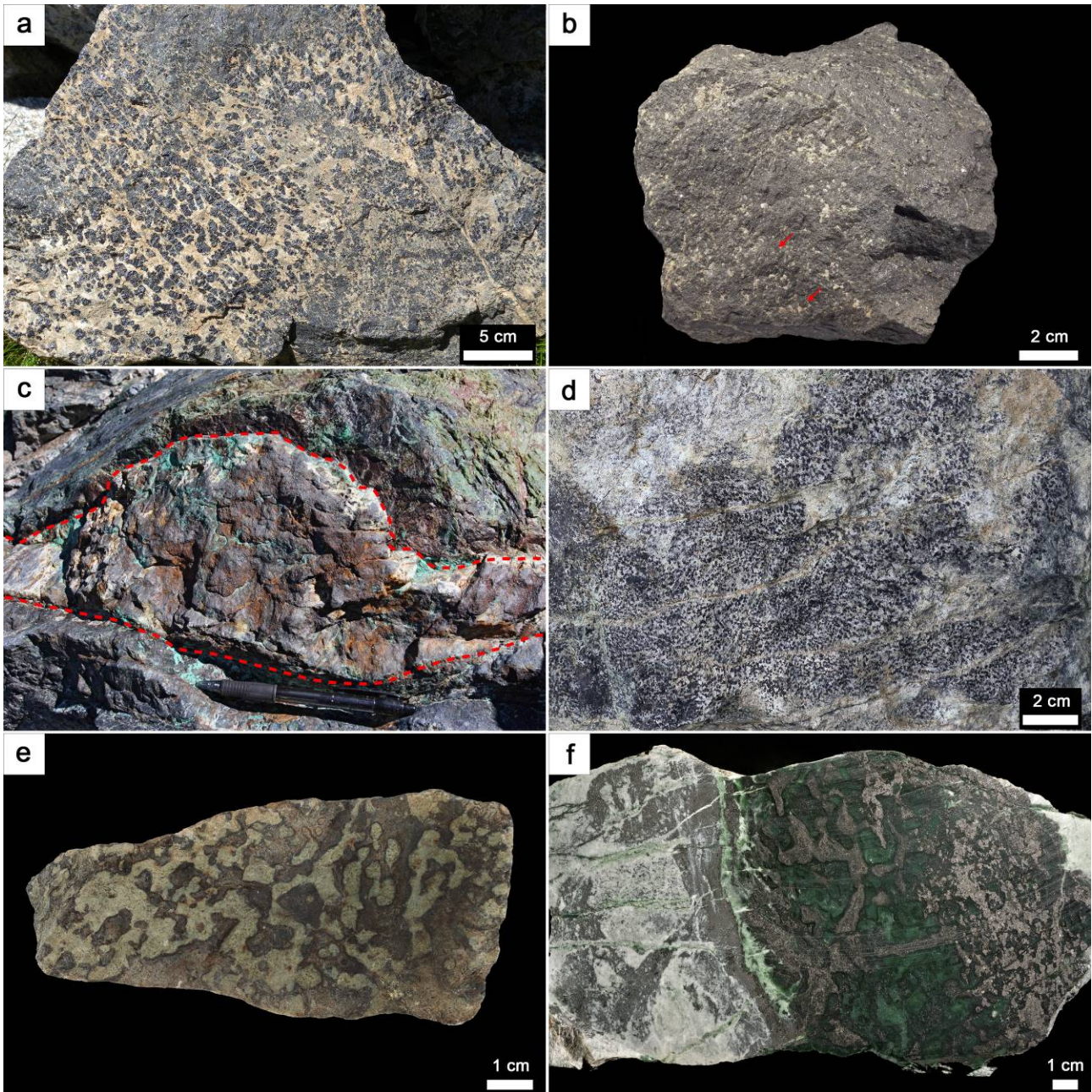


1360

1361

1362 **Fig. 2** 3D model of the Cogne mining district depicting the structural relationships between the Cogne  
 1363 serpentinite and the associated units. Numbers indicate the sampling sites (see text for details). Units  
 1364 after Dal Piaz et al. (2010).  
 1365



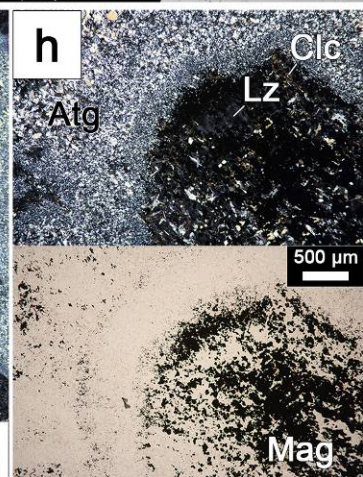
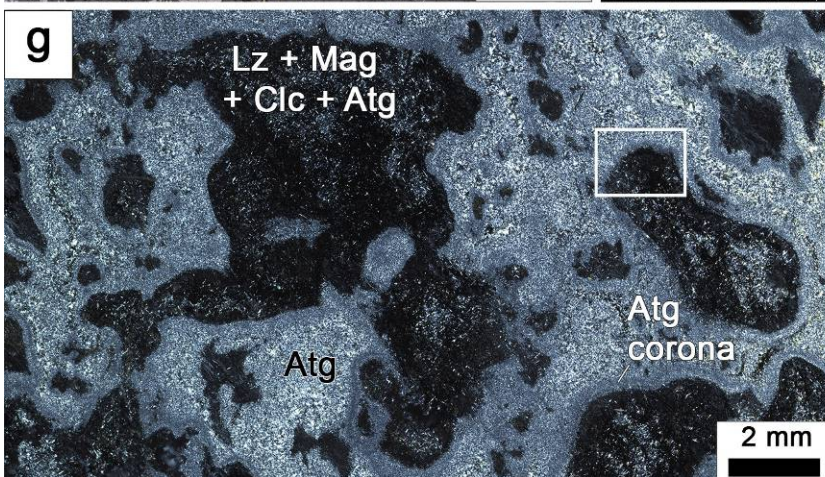
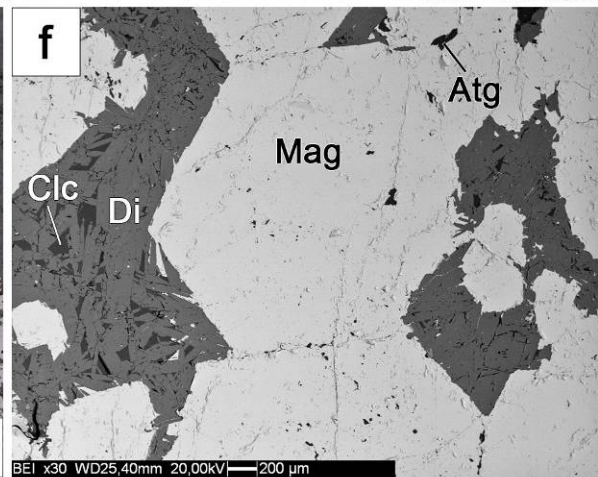
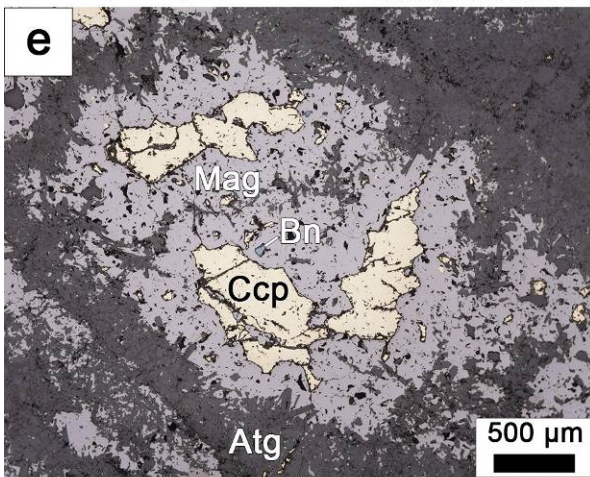
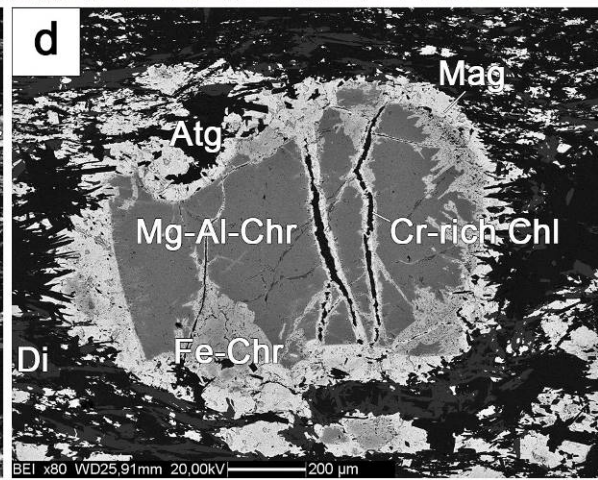
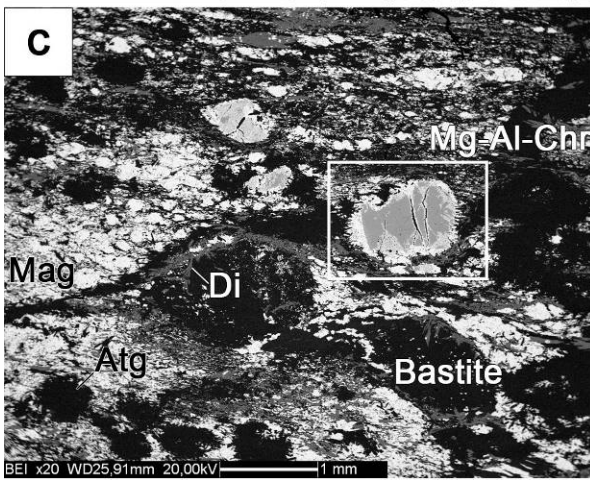
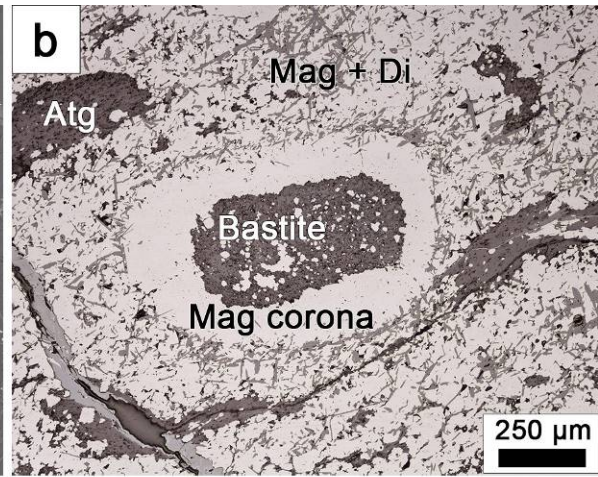
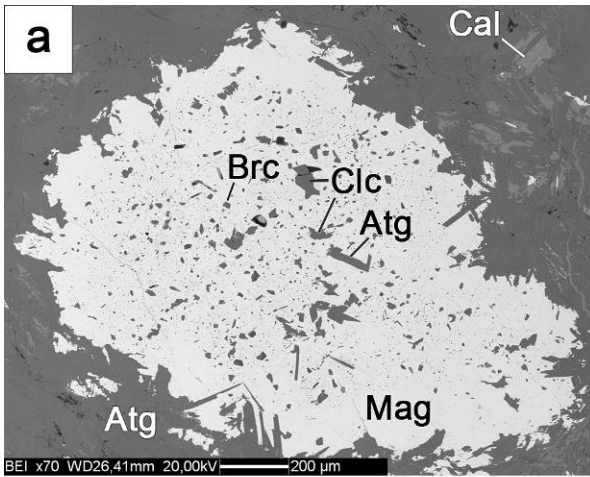


1366

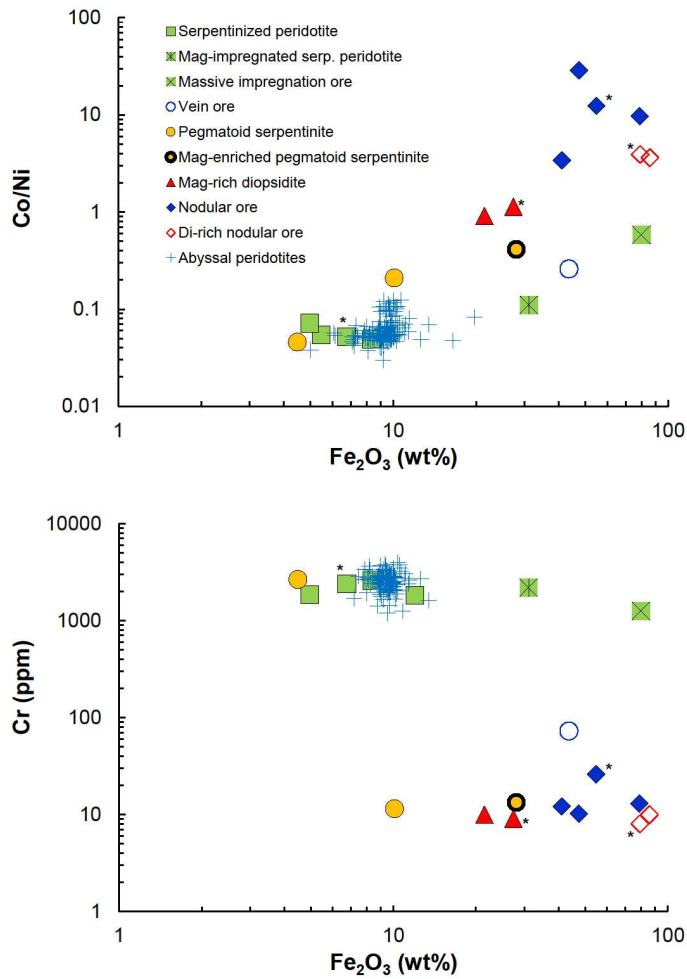
1367

1368 **Fig. 3** Typical ore and rock samples from Site 1 (a, b, c), Site 2 (d) and Site 3 (e, f). a) “Leopard” ore  
 1369 showing variation of texture at the sample scale. Dark areas are magnetite aggregates, the light portion  
 1370 is composed of serpentine and minor brucite and olivine. b) “Harrisitic” ore, characterized by  
 1371 elongated magnetite aggregates (dark areas) in serpentine (+ minor brucite and olivine) matrix. c)  
 1372 Massive magnetite ore, with minor serpentine gangue. d) Dismembered stockwork zone (outlined by  
 1373 dashed lines) in serpentinite after tectonic peridotite. Chalcopyrite is completely altered into Fe-  
 1374 oxyhydroxides and secondary copper minerals. The pen is 14 cm long. e) “Leopard” ore (right)  
 1375 grading to almost barren serpentinite. The rock is impregnated by diopside (whitish areas), which  
 1376 form patches and veinlets. The pen cap is 3 cm long. f) Serpentinized pegmatoid ultramafic rock  
 1377 variably enriched in magnetite (cut and polished sample). The left portion is a magnetite-rich  
 1378 diopside with relict brecciated texture.

1379

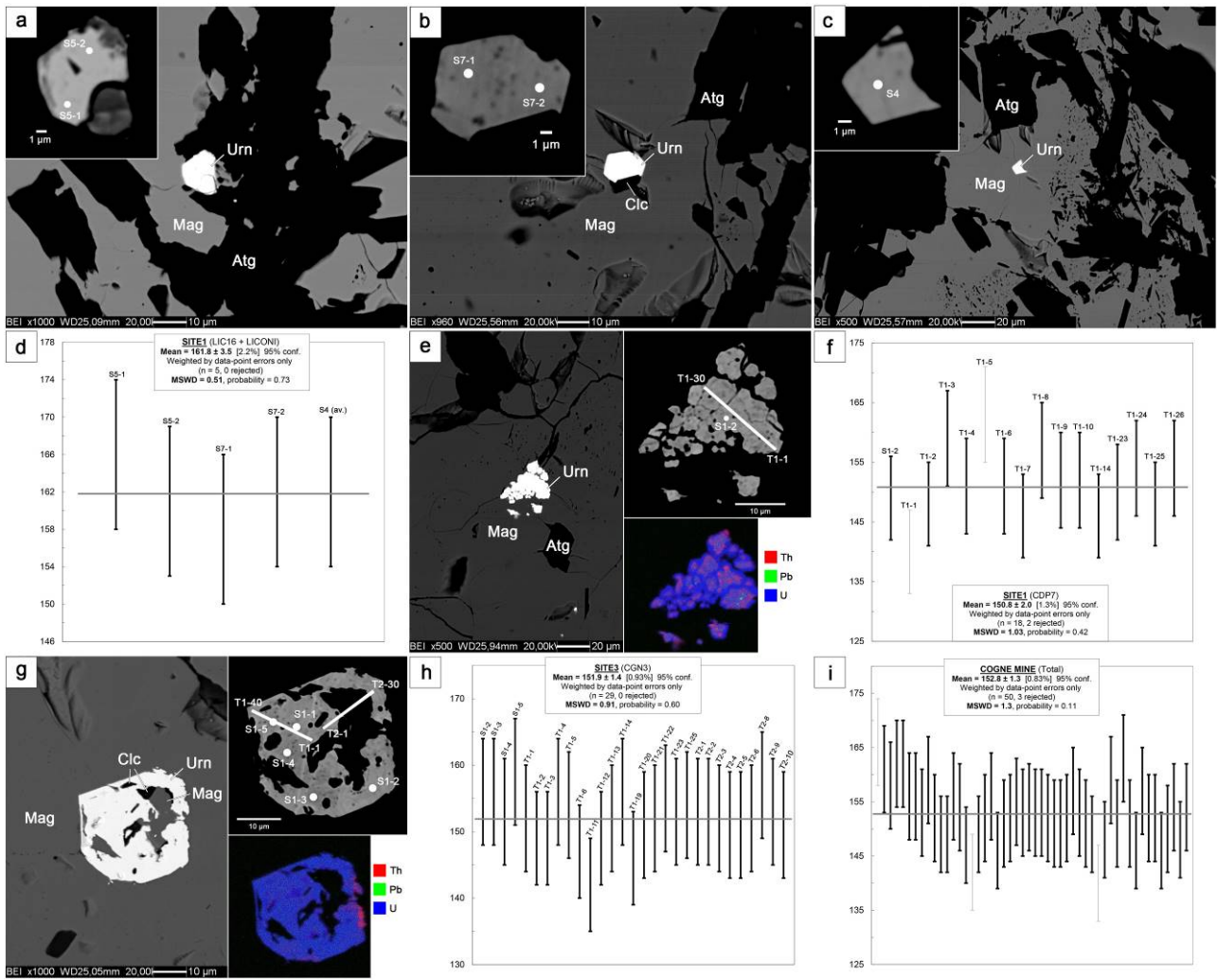


1382 **Fig. 4** Microstructural features in Cogne rocks. a) Magnetite poikiloblast in “leopard” ore from Site  
1383 1, showing indented boundaries with antigorite. Inclusions in magnetite are clinochlore (usually  
1384 anhedral), brucite (small and euhedral) and antigorite (large euhedral crystals). Gangue is antigorite.  
1385 Calcite forms late impregnations and veins. Back-scattered electron (BSE) image. b) Bastite with a  
1386 magnetite corona in massive magnetite (white) with acicular diopside (grey). Magnetite-impregnated  
1387 serpentized peridotite from Site 2. Reflected plane-polarized light. c) Magnetite-impregnated  
1388 serpentized peridotite from Site 2. Magnetite (white), antigorite (black) and diopside (medium grey)  
1389 replace former silicates, however bastite sites (round black areas) are still preserved. Mg-Al-chromite  
1390 (medium grey) is partly altered into ferrian chromite (light gray) + chlorite (black veins crosscutting  
1391 the crystal) and shows a rim of magnetite. BSE image. d) Magnetite + chalcopyrite dismembered vein  
1392 associated with antigorite from Site 2. Bluish inclusions in magnetite are bornite. Antigorite is both  
1393 included in magnetite or surrounds it forming indented boundaries. Reflected plane-polarized light.  
1394 e) External portion of a magnetite stockwork zone (located further to the left, not visible) from Site  
1395 2, in which an antigorite front replaces lizardite. White veins are Fe-oxyhydroxides produced by  
1396 weathering of chalcopyrite in the vein. BSE image. f) Euhedral magnetite crystals in a diopside-rich  
1397 portion of a “leopard” ore sample from Site 3. Diopside forms randomly-oriented subhedral prismatic  
1398 crystals (medium gray) with interstitial antigorite (dark grey). Black mineral included in magnetite  
1399 or interstitial between diopside crystals (right) is clinochlore. BSE image. g) Serpentinized pegmatoid  
1400 ultramafic rock from Site 3 (see Fig. 3f), showing an eutectic-like texture. Transmitted light, crossed  
1401 polars. h) Enlargement of framed area in c). Light-coloured domain (upper left) is composed of  
1402 coarse-grained interlocking antigorite; dark domain (right) is made up of isotropic lizardite,  
1403 clinochlore (anomalous brown interference colour), antigorite (white-light grey) and magnetite  
1404 (opaque). Fine-grained interlocking antigorite lines the boundary between the two domains.  
1405 Transmitted light, crossed polars (upper) and plane polarized light (lower). Mineral abbreviations  
1406 (after Whitney and Evans, 2010): Mag, magnetite; Atg, antigorite; Clc, clinochlore; Brc, brucite; Cal,  
1407 calcite; Di, diopside; Lz, lizardite; Ccp, chalcopyrite; Bn, bornite; Mg-Al-Chr, Mg-Al-chromite.  
1408



1410

1411 **Fig. 5** Cogne rocks plotted in a Co vs Ni plane and compared to abyssal ultramafic and mafic rocks  
 1412 and Fe-Ti gabbros from Valle d'Aosta ophiolites. Data for Cogne include compositions by Carbonin  
 1413 et al. (2014; marked with an asterisk). Data for abyssal peridotites after Niu (2004), Paulick et al.  
 1414 (2006), Andreani et al. (2014). Data for oceanic mafic intrusives after Casey (1997), Werner (1997),  
 1415 Holm (2002), Boschi et al. (2006), Paulick et al. (2006). Data for Fe-Ti gabbros after Bocchio et al.  
 1416 (2000).

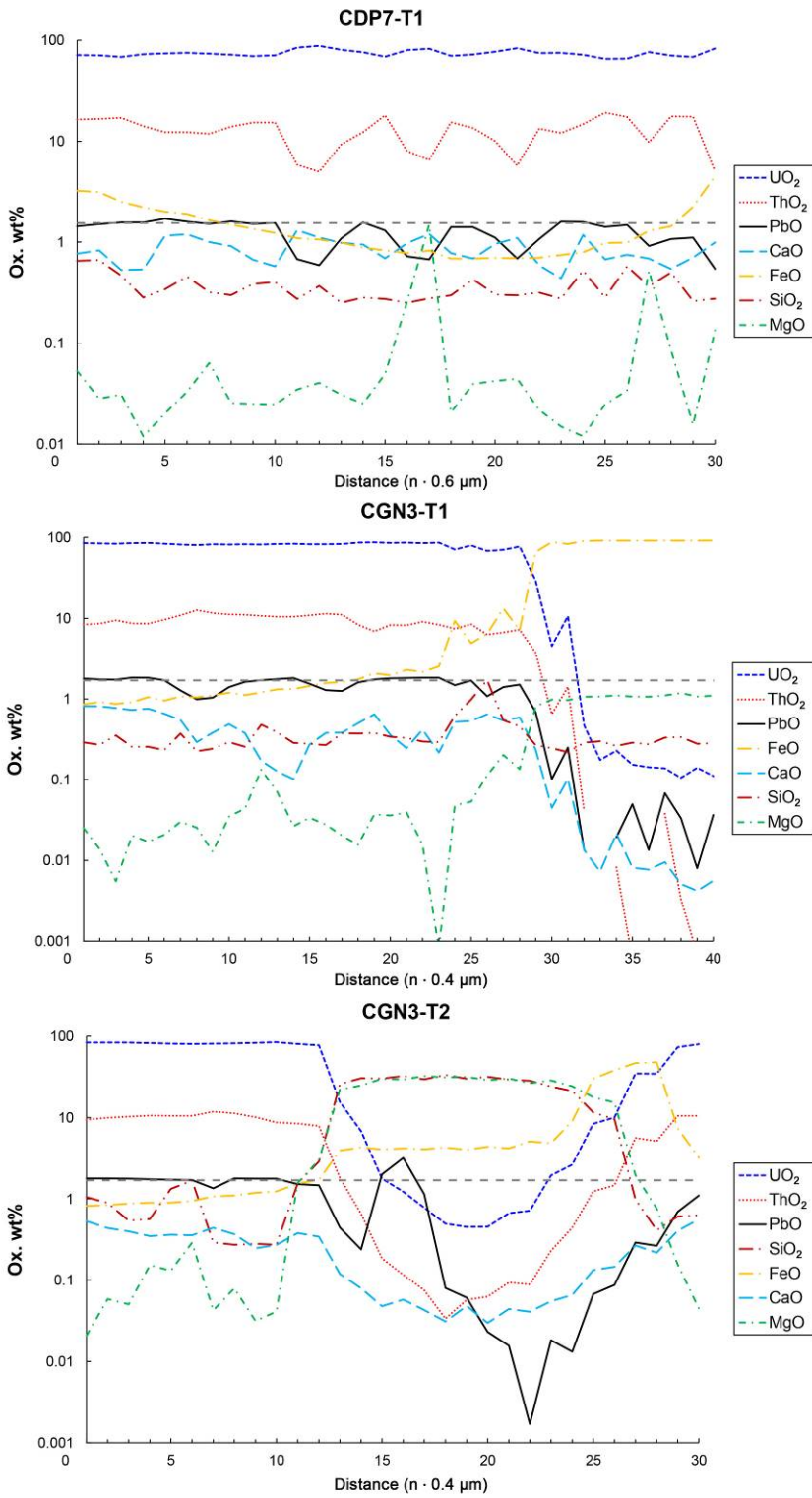


1417  
1418

1419

1420

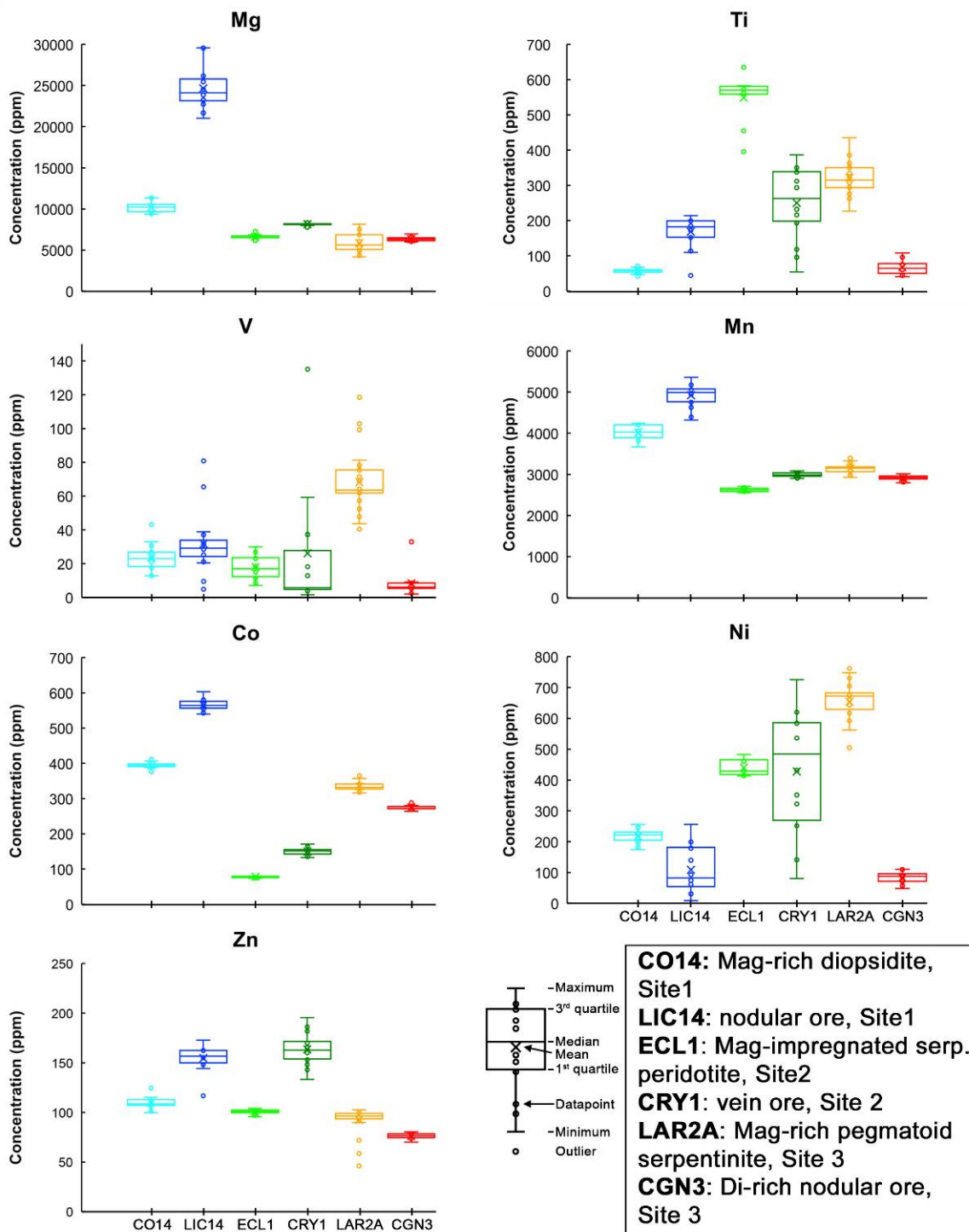
1421 **Fig. 6** Uraninite microstructural features and U-Th-Pb dating. a-d) Uraninite in Site 1 “leopard” ore  
 1422 and related dating [b) and c) from the same ore sample]. e-f) Aggregate of uraninite crystals in Site 1  
 1423 “leopard” ore and related dating. Chemical map shows a U-rich rim. g-h) Inclusion-rich (magnetite,  
 1424 dark grey; clinocllore, black) uraninite crystal in Site 3 “leopard” ore and related dating. The  
 1425 chemical map reveals a homogeneous composition. i) Combination of all single-spot datings. Images  
 1426 and maps were obtained by SEM-BSE and EPMA, respectively. Geochronological data plotted using  
 1427 ISOPLOT (v. 3.75) Visual Basic add-in for Excel® (Ludwig 2012).  
 1428



1429

1430 **Fig. 7** Electron microprobe traverses across uraninite crystals (see Fig. 6). Horizontal dashed lines  
 1431 indicate PbO plateau.

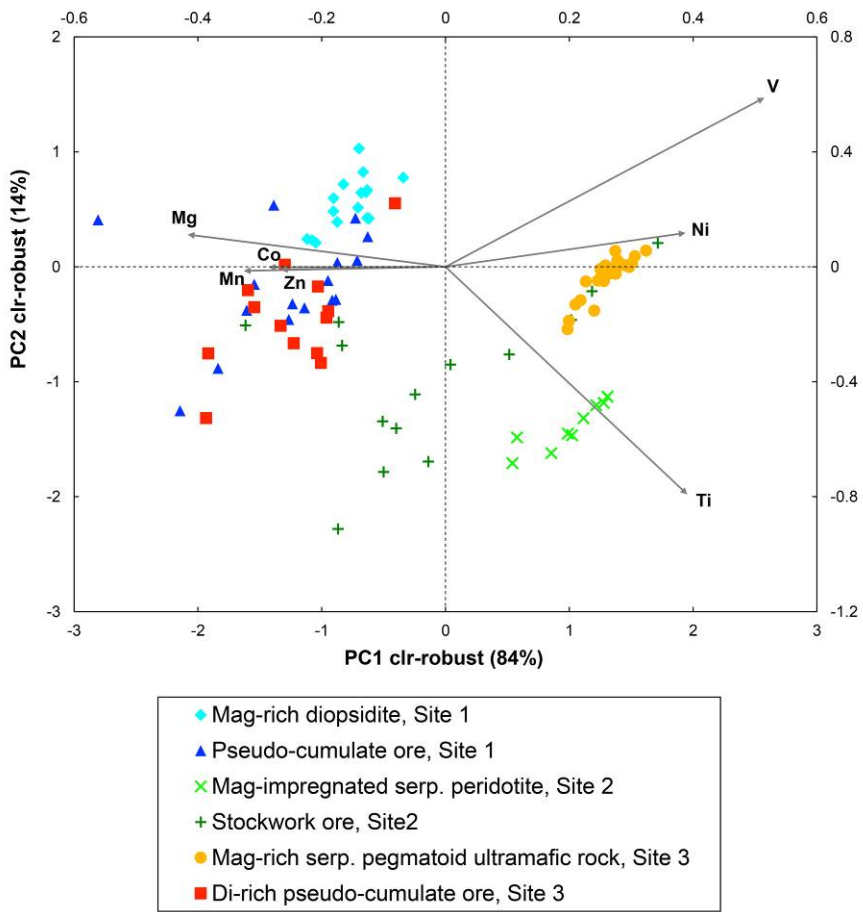
1432



1433

1434 **Fig. 8** Box and whiskers plot of magnetite trace element composition. “X” symbol indicates the  
 1435 arithmetic mean.

1436

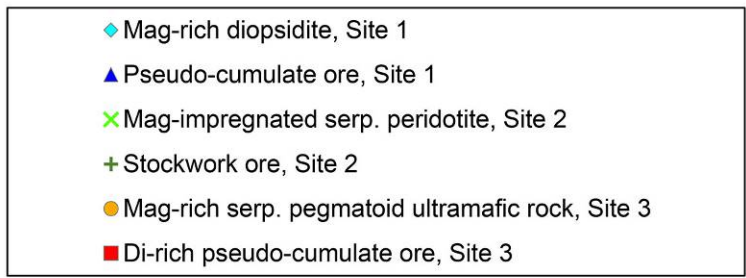
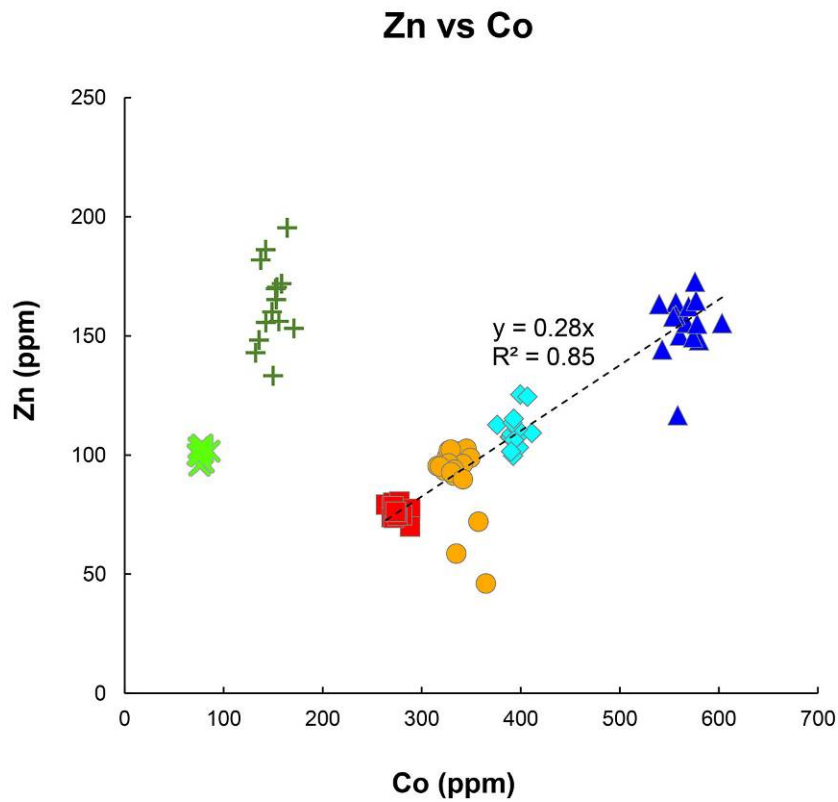


1437

1438

1439 **Fig. 9** Robust-PCA of magnetite trace element composition. Coordinates of datapoints (scores) are  
 1440 on left and lower horizontal axes. Coordinates of variables (loadings) are on right and upper  
 1441 horizontal axes.  
 1442



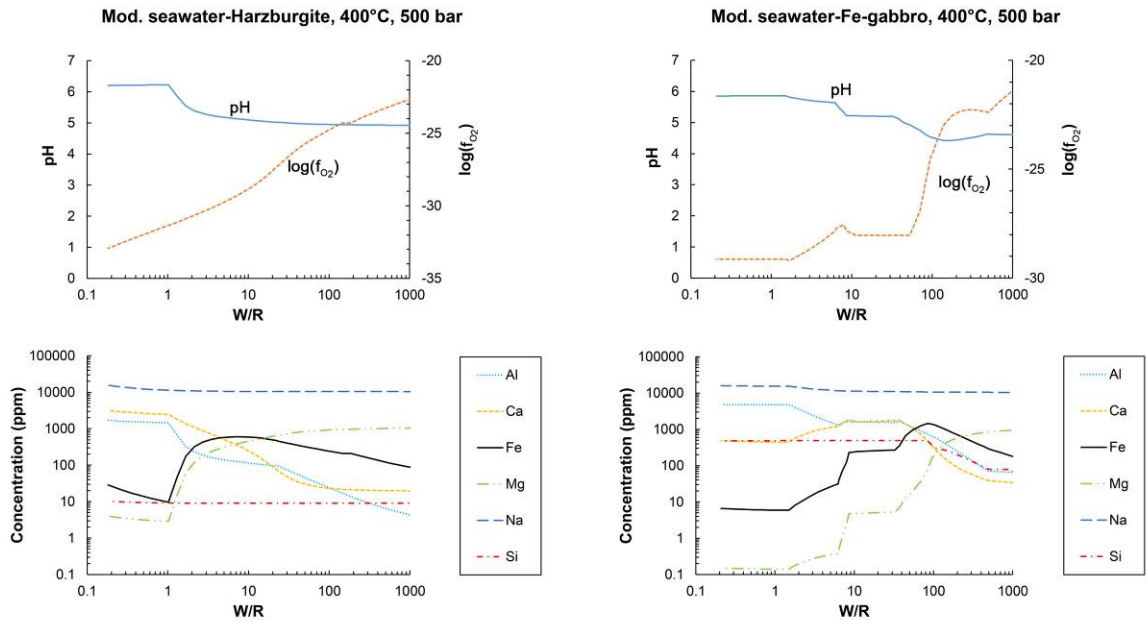


1443

1444

1445 **Fig. 10** Co vs. Ni relationships in magnetite. Regression line (dashed) for magnetite-rich samples  
 1446 from Site 1 and 3 shows linear relationship between Co and Ni.

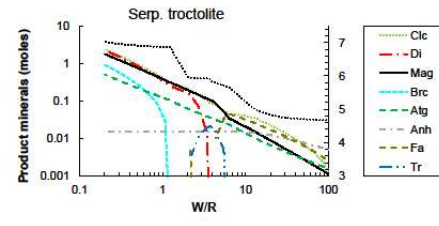
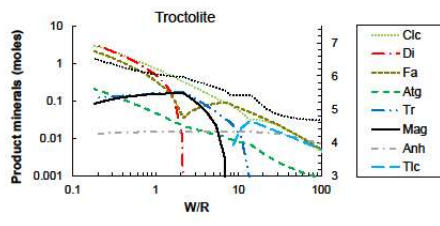
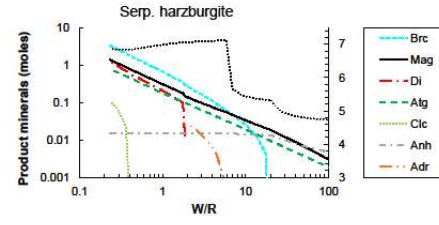
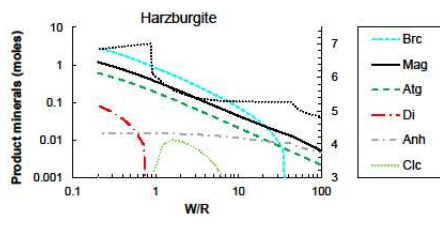
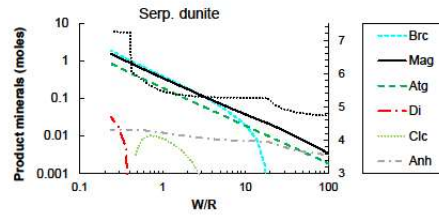
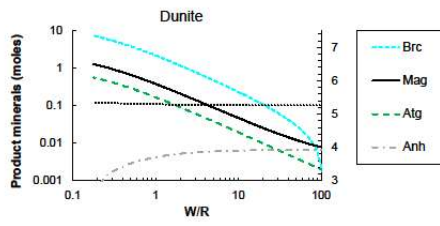
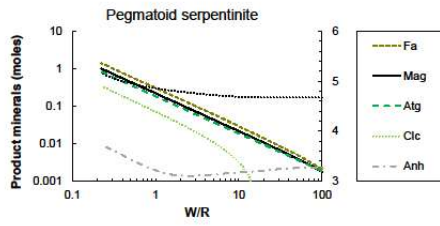
1447



1448

1449

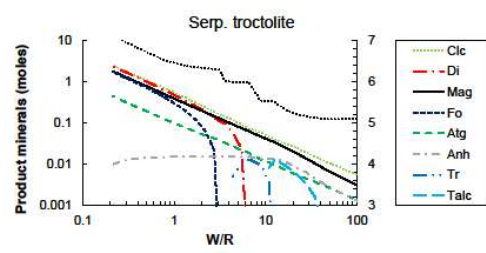
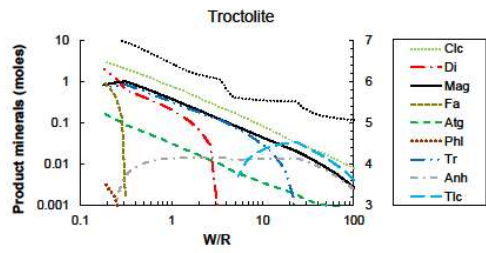
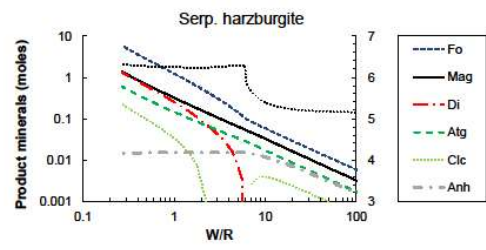
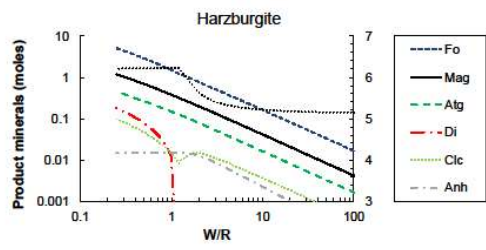
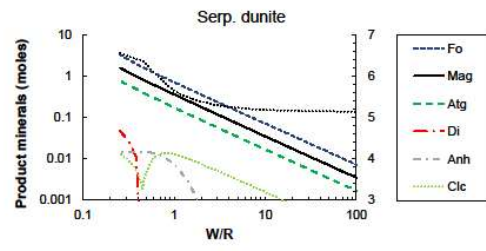
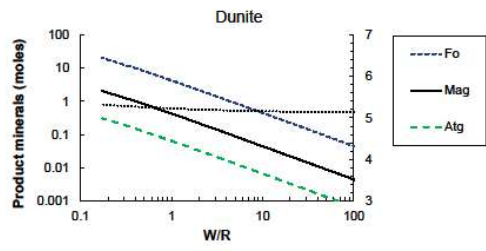
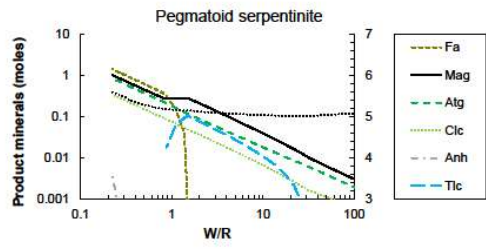
1450 **Fig. 11** Variation in pH,  $f_{O_2}$  and element concentrations in fluid equilibrated with harzburgite (a, c)  
 1451 or Fe-gabbro (b, d) at 400°C at various W/R.  
 1452



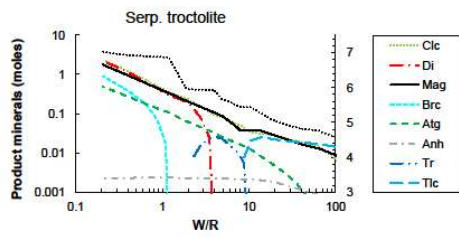
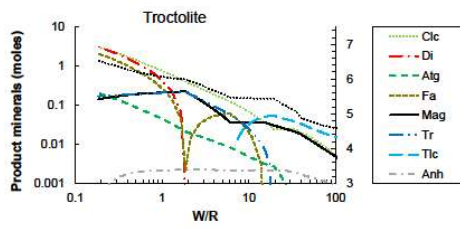
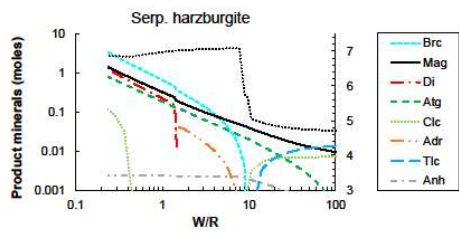
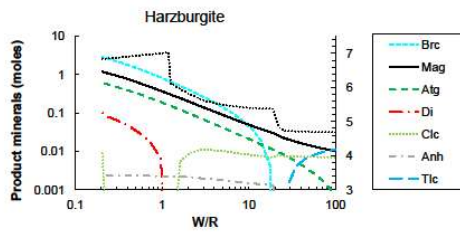
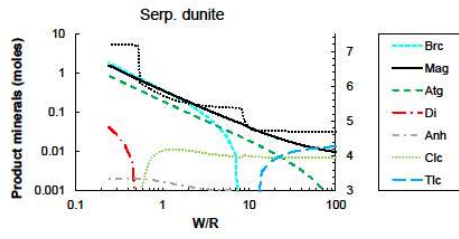
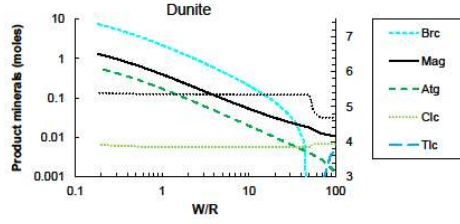
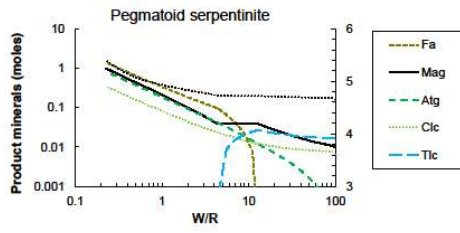
1453

1454

1455

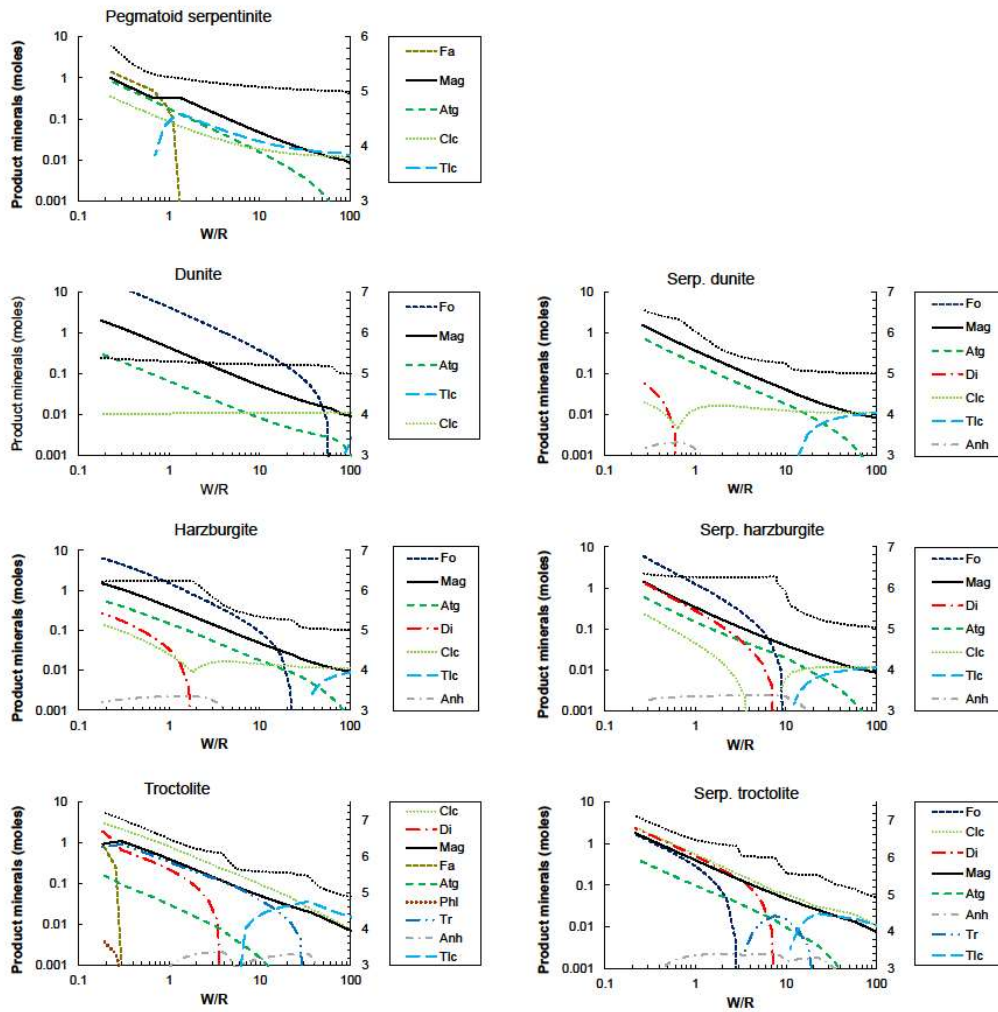






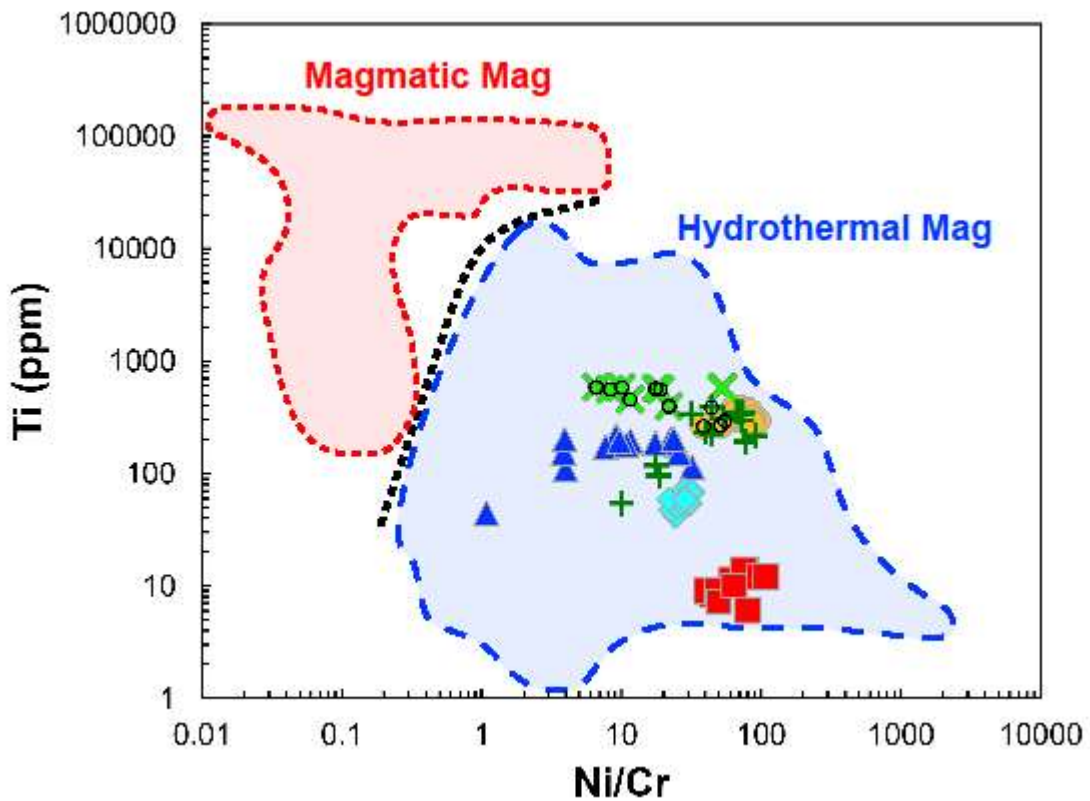
1458

1459



1460

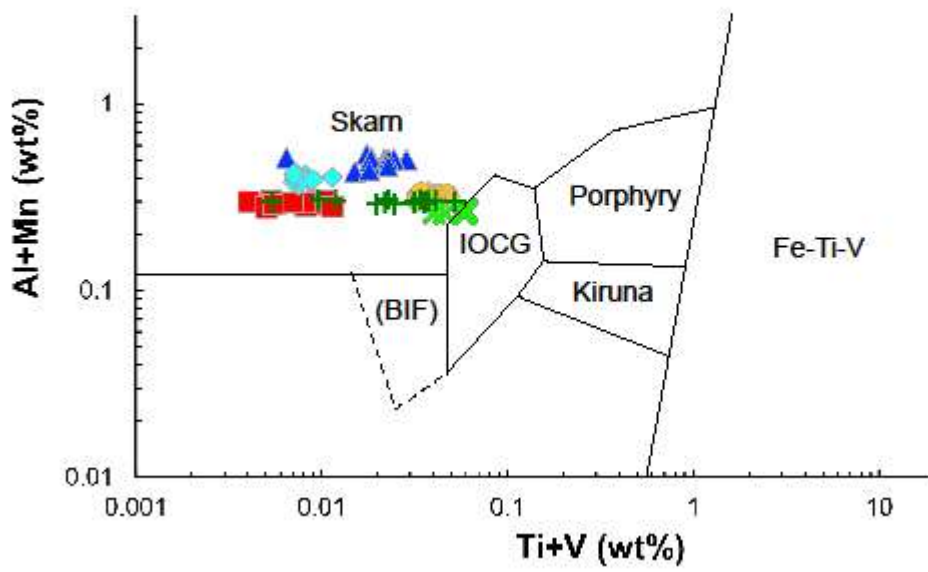
1461 **Fig. 12** Mineral assemblages produced by reaction of model hydrothermal fluids with selected rock  
 1462 types. Harzburgite-reacted fluid reacting with rocks at a) 300°C and 500 bar c) 400°C and 500 bar.  
 1463 Fe-gabbro-reacted fluid reacting with rocks at b) 300°C and 500 bar d) 400°C and 500 bar.  
 1464



1465

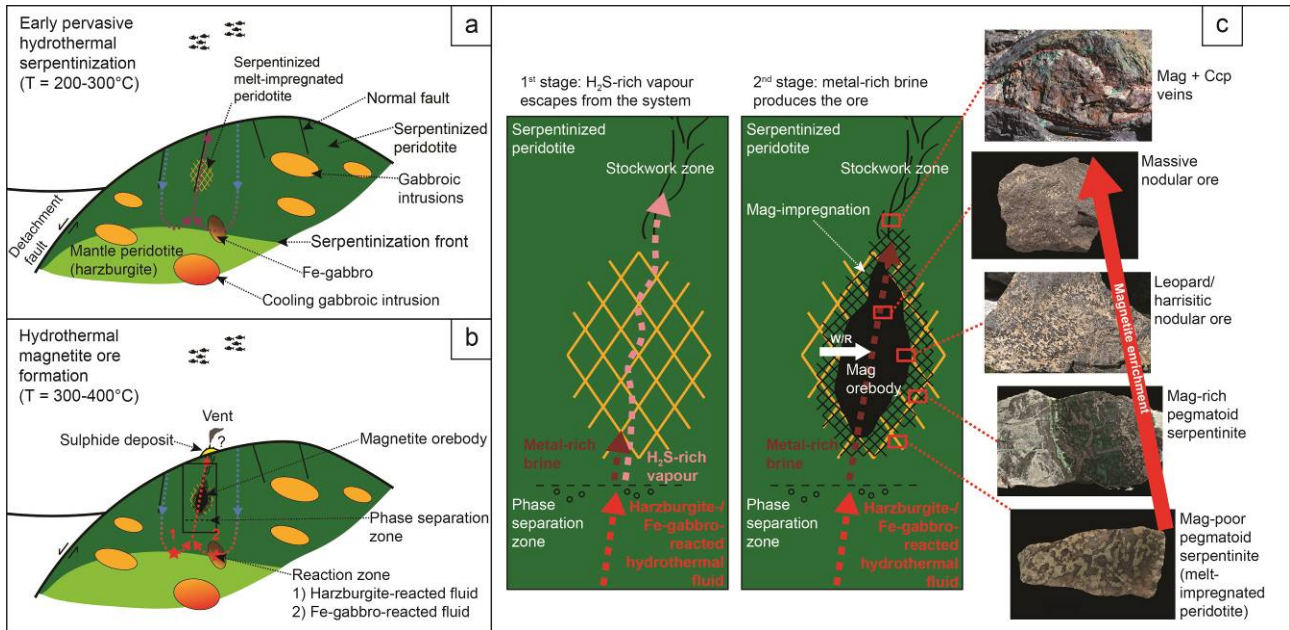
1466 **Fig. 13.** Compositions of Cogne magnetites plotted in the discrimination diagram by Dare et al.  
 1467 (2014). Magnetites with Cr contents above detection limit are circled. The other data points are  
 1468 plotted assuming a Cr value equal to the detection limit of 8 ppm. Although this may have unduly  
 1469 shifted the points to lower Ni/Cr ratios, the strong hydrothermal character of the Cogne magnetites  
 1470 remains evident.





1471

1472 Fig. 14. Compositions of Cogne magnetites in the discrimination diagram of Dupuis and Beaudoin,  
 1473 2011. LA-ICP-MS data are not available for Al (generally  $\ll 0.1$  wt% based on EPMA data),  
 1474 therefore the plotted (Mn + Al) contents should be considered as minimum values.



1475

1476 **Fig. 15.** Interpreted schematic evolution of the Cogne deposit. a) Formation of an oceanic core  
 1477 complex made up of mantle peridotites intruded by gabbros and Fe-gabbros, and locally impregnated  
 1478 by melts. Early circulation of hydrothermal fluids produces extensive serpentinization at relatively  
 1479 low-T (lizardite stability field). High water/rock ratios are possibly attained thanks to fluid focussing  
 1480 along fractures and faults. b) Convective circulation of seawater produces high-T hydrothermal fluids  
 1481 that leach metals from harzburgites and Fe-gabbros. These fluids undergo phase separation and  
 1482 produce a magnetite-rich body at depth and a sulphide mound on the seafloor. A magnetite-sulphide  
 1483 stockwork zone marks the transition between the magnetite orebody and the sulphide mound. c)  
 1484 Close-up of the framed region in b). Phase separation produces an H<sub>2</sub>S-rich vapour that quickly  
 1485 escapes from the system and a dense metal-rich brine. Then, the upwelling brine reacts with the  
 1486 serpentinites at various fluid/rock ratios and precipitates magnetite, producing fine-grained  
 1487 disseminated, nodular and replacive massive ores. Further upwelling of the magnetite-saturated fluids  
 1488 along fractures produces magnetite + chalcopyrite veins (stockwork zone) and fine-grained  
 1489 disseminations in shallower serpentinites.

Rock Type	Fe-gabbro <sup>1</sup>	Dunite <sup>1</sup>	Serp. Dunite <sup>2</sup>	Harzburgite <sup>1</sup>	Serp. Harzburgite <sup>2</sup>	Cumulate Harzburgite <sup>3</sup>	Serp. Cumulate Harzburgite <sup>3</sup>	Troctolite <sup>1</sup>	Serp. Troctolite <sup>4</sup>
Ox. wt%									
SiO <sub>2</sub>	47.94	40.87	39.24	44.31	39.38	47.09	38.98	42.90	37.95
Al <sub>2</sub> O <sub>3</sub>	12.19	0.00	0.19	0.42	0.59	1.30	0.71	9.58	6.12
FeO	18.87	9.77	7.57	8.97	6.61	6.74	6.24	9.06	8.44
MgO	4.85	49.35	38.79	45.81	38.37	44.20	40.31	32.39	34.73
CaO	13.17	0.00	0.08	0.48	1.69	0.68	0.21	5.39	2.87
Na <sub>2</sub> O	2.99	0.00	0.13	0.00	0.05	0.00	0.00	0.67	0.41
H <sub>2</sub> O	0.00	0.00	13.99	0.00	13.30	0.00	13.55	0.00	9.47
Tot.	100.00	100.00	100.00	100.00	100.00	100.00	100.00	100.00	100.00

---

<sup>1</sup> "Artificial" rock

<sup>2</sup> Andreani et al. (2014)

<sup>3</sup> Paulick et al. (2006)

<sup>4</sup> Sanfilippo et al. (2014)



Location	Site 1	Site 1	Site 1	Site 1	Site 2	Site 2	Site 3	Site 3	Site 3	Site 3	Site 3
Sample	LIC1B	LIC12*	LIC14*	LIC15	ECL1*	CRY1	LAR4	LAR2-1*	LAR2-2*	CGN3*	CGN8*
Rock type	Serpentinite	Serpentinite (harzburgite)	Pseudo-cumulate ore	Pseudo-cumulate ore	Mag-impregnated serp. peridotite	Stockwork ore	Serpentinite	Mag-rich serp. pegmatoid ultramafic rock	Mag-rich diopsidite	Di-rich pseudo-cumulate ore	Pseudo-cumulate ore
Ox. wt%											
SiO <sub>2</sub>	41.91	39.49	22.38	20.51	32.20	24.60	39.06	33.14	42.40	6.52	10.06
TiO <sub>2</sub>	0.02	0.02	0.06	0.02	0.04	0.04	0.10	0.03	0.02	0.02	0.02
Al <sub>2</sub> O <sub>3</sub>	1.04	1.01	0.62	1.08	0.92	0.43	2.67	2.31	0.27	0.86	0.31
Fe <sub>2</sub> O <sub>3</sub>	5.46	8.31	41.04	47.34	31.09	43.44	4.94	28.03	21.44	85.73	78.70
MgO	38.28	37.57	28.22	21.07	25.72	22.35	33.39	30.69	16.01	3.90	9.17
MnO	0.11	0.10	0.31	0.31	0.17	0.20	0.16	0.17	0.17	0.35	0.40
CaO	0.26	0.02	0.11	2.21	2.63	0.04	5.84	0.14	18.19	1.50	0.03
Na <sub>2</sub> O	0.04	0.03	0.02	0.02	0.03	0.02	0.03	0.04	0.02	0.02	0.01
K <sub>2</sub> O	0.01	0.01	0.01	0.01	0.01	0.00	0.01	0.01	0.01	0.01	0.01
P <sub>2</sub> O <sub>5</sub>	0.01	0.01	0.02	0.01	0.01	0.01	0.01	0.01	0.01	0.02	0.01
LOI	12.19	12.57	6.88	7.09	7.09	6.75	13.21	5.18	98.54	0.21	0.32
Total	99.32	99.14	99.66	99.66	99.90	97.87	99.42	99.76	0.72	99.13	99.04
ppm											
Be	-	<1	<1	-	1.00	-	-	<1	<1	<1	<1
S	53	1194	245	193	948	3290	946	124	104	14	6
Sc	BDL	6	<1	BDL	6	BDL	BDL	2	1	<1	<1
V	31	26	<8	BDL	31	55	47	20	12	<8	<8
Cr	2391	2395	<14	BDL	2196	78	2132	<14	<14	21	<14
Co	87.0	117.4	236.8	345.0	97.8	133.0	111.0	105.8	72.3	260.9	295.2
Ni	1596	2403	93	12	1005	511	1542	275	97	110	42
Cu	22	20	36	29	209	14659	23	70	77	45	38
Zn	47	54	82	111	129	140	44	66	38	83	84
Ga	BDL	0.8	1.3	BDL	<0.5	BDL	BDL	8.3	2.0	3.5	0.8
Rb	BDL	<0.1	<0.1	BDL	<0.1	BDL	BDL	0.1	<0.1	<0.1	<0.1
Sr	BDL	<0.5	1.3	87.0	1.0	BDL	115.0	<0.5	12.4	1.8	0.6
Y	BDL	0.5	0.5	BDL	0.2	BDL	BDL	1.0	3.4	0.5	0.4
Zr	BDL	3.4	5.8	BDL	0.7	BDL	BDL	1.9	2.8	1.0	0.8
Nb	BDL	<0.1	0.6	BDL	<0.1	BDL	BDL	<0.1	0.9	0.4	<0.1
Sn	-	<1	<1	-	<1	-	-	<1	<1	<1	<1
Cs	-	<0.1	<0.1	-	<0.1	-	-	<0.1	<0.1	<0.1	<0.1
Ba	BDL	1.0	<1	BDL	<1	BDL	17.0	1.0	3.0	<1	<1
Hf	-	<0.1	0.2	-	<0.1	-	-	<0.1	0.1	<0.1	<0.1
Ta	-	<0.1	<0.1	-	<0.1	-	-	<0.1	<0.1	<0.1	<0.1
W	-	1.1	4.0	-	<0.5	-	-	<0.5	<0.5	<0.5	<0.5
Pb	9.0	38.0	16.0	10.0	10.0	20.0	16.0	29.0	22.0	10.0	BDL
Th	BDL	<0.2	0.9	BDL	<0.2	BDL	BDL	0.3	0.5	<0.2	<0.2
U	BDL	<0.1	2.9	BDL	<0.1	BDL	BDL	1.3	2.0	0.8	2.4
La	BDL	0.9	0.4	BDL	0.2	BDL	BDL	0.8	3.3	0.9	0.3
Ce	BDL	0.7	0.6	BDL	0.1	BDL	BDL	0.9	5.8	1.1	0.7
Nd	BDL	0.4	0.7	BDL	<0.3	BDL	BDL	0.3	3.8	0.7	0.4

\* integrated with data from ICP-MS





Hydrothermal fluids

	Harzburgite- reacted	Fe-gabbro- reacted	Rainbow
Na	459.0	456.4	570.0
Ca	19.3	5.4	67.7
Mg	12.4	14.4	1.7
Si	0.3	18.4	7.3
Fe	2.0	10.4	22.2
Al	0.0019	0.0023	0.0029
Cl	535.3	523.9	757.0

---